



Forschungszentrum Karlsruhe
in der Helmholtz-Gemeinschaft

Wissenschaftliche Berichte
FZKA 6914

**Limit Strains for
Severe Accident Conditions
Synthesis Report of the
EU-project LISSAC
Contract No. FIKS-CT1999-00012**

Compiled by

R. Krieg
Programm Nukleare Sicherheitsforschung

M. Seidenfuß
Staatliche Materialprüfungsanstalt,
Universität Stuttgart

Oktober 2003

Forschungszentrum Karlsruhe

in der Helmholtz-Gemeinschaft

Wissenschaftliche Berichte

FZKA 6914

Limit Strains for Severe Accident Conditions

Synthesis Report of the EU-project LISSAC

Contract No. FIKS-CT1999-00012

Compiled by

R. Krieg

Co-ordinator of the Project

Programm Nukleare Sicherheitsforschung

and

M. Seidenfuß

Staatliche Materialprüfungsanstalt, Universität Stuttgart

Forschungszentrum Karlsruhe GmbH, Karlsruhe

2003

Impressum der Print-Ausgabe:

**Als Manuskript gedruckt
Für diesen Bericht behalten wir uns alle Rechte vor**

**Forschungszentrum Karlsruhe GmbH
Postfach 3640, 76021 Karlsruhe**

**Mitglied der Hermann von Helmholtz-Gemeinschaft
Deutscher Forschungszentren (HGF)**

ISSN 0947-8620

Contributions by

B. Dolensky, T. Jordan, M. Lux, T. Malmberg, G. Messemer, H. Rieger,
Forschungszentrum Karlsruhe (FZK/IRS);

J. Aktaa, E. Diegele, D. Hofer, Mrs. E. Materna-Morris, R. Schmitt,
Forschungszentrum Karlsruhe (FZK/IMF);

P. Julisch, H.-J. Hädrich, H.-P. Seebich,
Staatliche Materialprüfungsanstalt Stuttgart (MPA);

D. Kalkhof,
Paul Scherrer Institut (PSI);

Mrs. H. Talja, H. Keinänen, P. H. Pankakoski,
Technical Research Centre of Finland (VTT);

G. Solomos, E. Pizzinato,
European Commission, Joint Research Centre Ispra (JRC);

E. Aifantis, I. Tsagrakis,
Aristotle University of Thessaloniki (AUT);

L. Cizelj, M. Kovac,
Institut Jozef Stefan (IJS);

C. Caroli,
Ente per le Nuove tecnologie, l'Energia e l'Ambiente (ENEA);

J. H. Fokkens, J. M. Church, S. de Groot,
Nuclear Research and consultancy Group (NRG);

S. Bhandari, C. Benhamou, K. Schramm,
Framatome ANP (Framatome);

P. Verón,
Equipos Nucleares S.A. (ENSA);

R. Kieselbach, G. Hartmann,
Swiss Federal Laboratories for Material Research (EMPA);

Support for preparation of this report:

G. Hailfinger, FZK/IRS

Administrative matters:

H. Plitz, FZK/NUKLEAR

SUMMARY

The local failure strains of essential reactor vessel components are investigated. The size influence of the components is of special interest. Typical severe accident conditions including elevated temperatures and dynamic loads are considered.

The main part of work consists of test families with specimens under uniaxial and biaxial static and dynamic loads. Within one test family the specimen geometry and the load conditions are similar, the temperature is the same; but the size is varied up to reactor dimensions. Special attention is given to geometries with a hole or a notch causing non-uniform stress and strain distributions typical for reactor components.

To manufacture all specimens sufficient material was available from the unused reactor pressure vessel Biblis C. Thus variations of the mechanical material properties, which could impair the interpretation of the test results, are rather small. This has been confirmed by an adequate number of additional quality assurance tests.

A key problem was to determine the local strain at failure. Here suitable methods had to be developed including the so-called "vanishing gap method" and the "forging die method". They are based on post test geometrical measurements of the fracture surfaces and reconstructions of the related strain fields using finite element calculations, for instance.

To deepen the understanding of structural degradation and fracture and to allow extrapolations, advanced computational methods including damage models have been developed and validated. Several approaches were tried in parallel including so-called non-local concepts and descriptions of stochastic properties at grain size level.

The experimental results indicate that stresses versus dimensionless deformations are approximately size independent up to failure for specimens of similar geometry under similar load conditions. Also the maximum stress is approximately size independent, if failure occurs after the maximum stress is reached.

Cracks are initiated, if the local equivalent strain reaches a critical value, called the local failure strain. It turned out to be more than 50 % for large specimens approaching the dimensions of the reactor pressure vessel.

The local failure strains are size dependent. They reach values around 150 % for small specimens with thicknesses or diameters of a few millimetres.

The parameter describing the size effect is the radius of holes or notches located in critical specimen regions. The shape of the specimen and the type of load plays a minor role.

The scatter of the results on structural failure is considerable. However statistical evaluations indicate that the failure strain will hardly fall below a lower threshold.

Thus limit strains, depending on the hole or notch radius in the critical specimen region could be proposed for temperatures up to 400 °C. Dynamic loads are included. Limit strains for higher temperatures up to 850 °C are also discussed.

Using the limit strains a more realistic strain based concept can be employed for analyses of severe accident consequences. Furthermore the results on size effects will help to examine, whether findings from small scale model experiments can be converted to reactor conditions.

The applicability of the results can be extended to other geometries and load conditions by using recommended theoretical models. However, in any case, care must be taken when the stress triaxiality is higher than in the tested specimens. In this case the failure strain may decrease significantly.

Application of the proposed limit strains to selected severe accident problems shows that the admissible load increases by a factor between 1.25 and about 2.0 in comparison to using state-of-the-art rules.

A more detailed report has been published as FZKA 6854.

Dehnungsgrenzen für Materialbeanspruchungen bei schweren Unfällen

ZUSAMMENFASSUNG

Die lokalen Versagensdehnungen wesentlicher Komponenten des Reaktordruckbehälters werden untersucht. Der Größeneinfluss der Komponenten ist von besonderem Interesse. Typische Unfallbedingungen wie erhöhte Temperaturen und dynamische Beanspruchungen werden berücksichtigt.

Hauptteil der Arbeiten sind Testfamilien mit Materialproben unter ein- und mehrachsiger statischer und dynamischer Belastung. Innerhalb einer Testfamilie ist die Probengeometrie ähnlich und die Temperatur ist gleich; nur die Probengröße wird variiert bis hin zu Reaktorabmessungen. Die meisten Proben enthalten ein Loch oder eine gerundete Kerbe. Die dadurch hervorgerufenen ungleichmäßigen Spannungs- und Dehnungsverteilungen sind typisch für Reaktorkomponenten.

Zur Herstellung der Proben stand Material von dem nicht benutzten Reaktordruckbehälter Biblis C zur Verfügung. Dadurch war es möglich, die störenden Variationen der mechanischen Materialeigenschaften klein zu halten. Dies wird durch begleitende Materialstichproben bestätigt.

Ein Schlüsselproblem war die Bestimmung der lokalen Versagensdehnung. Hierzu mussten spezielle Methoden wie zum Beispiel die „vanishing gap method“ oder die „forging die method“ entwickelt werden. Sie beinhalten geometrische Vermessungen der Bruchoberflächen nach den Tests und erlauben die Rekonstruktion der Dehnungsfelder in den Proben während des Rissbeginns – beispielsweise mit Hilfe von Finite-Elemente-Rechnungen.

Um das Verständnis der beobachteten Materialschädigungen und der Bruchvorgänge zu vertiefen, wurden fortgeschrittene theoretische Modelle entwickelt und – wenn möglich – validiert. Dazu gehören unter anderem so genannte „non-local concepts“, aber auch Modelle, die die stochastischen Materialeigenschaften der einzelnen Körner berücksichtigen. Derartige Modelle sind bei der Extrapolation zu anderen Beanspruchungsbedingungen hilfreich.

Die experimentellen Ergebnisse zeigen, dass für ähnliche Probengeometrien und Belastungsbedingungen die Spannungen über den dimensionslosen Verformungen nahezu größenunabhängig sind – bis zu den jeweiligen größenabhängigen Versagenspunkten. Damit ist auch die Maximalspannung näherungsweise größenunabhängig, vorausgesetzt Versagen erfolgt nachdem die Maximalspannung erreicht wurde.

Risse werden initiiert, wenn die lokale Vergleichsdehnung einen kritischen Wert erreicht. Dieser kritische Wert wird als lokale Versagensdehnung definiert. Für große Proben im Bereich der Reaktorabmessungen beträgt sie mehr als 50%.

Die lokale Versagensdehnung ist größenabhängig. Für kleine Proben mit Dicken oder Durchmessern im Millimeterbereich erreicht sie etwa 150%.

Der die Probengröße beschreibende Parameter ist der Radius der Löcher und Kerben in den Proben. Die sonstige Form der Proben und die Art der Belastung hat dagegen nur geringen Einfluss.

Die Streuungen der ermittelten lokalen Versagensdehnungen sind erheblich. Statistische Bewertungen zeigen jedoch, dass die lokale Versagensdehnungen einen unteren größenabhängigen Grenzwert nicht unterschreiten.

Damit war es möglich größenabhängige, d.h. vom Loch- oder Kerbradius abhängige Dehnungsgrenzen vorzuschlagen. Temperaturvariationen zwischen Raumtemperatur und 400 °C sowie dynamische Berstungen sind erlaubt. Dehnungsgrenzen für höhere Temperaturen bis 850 °C werden diskutiert.

Mit Hilfe von Dehnungsgrenzen ist es möglich für schwere Unfälle ein wesentlich realistischeres, auf Dehnungen basierendes Bewertungskonzept anzuwenden. Ferner ist es jetzt möglich zu entscheiden, inwieweit experimentelle Ergebnisse von kleineren Reaktormodellen auf reale Reaktorabmessungen übertragen werden können.

Unter Beachtung der theoretischen Untersuchungen sind auch Anwendungen auf andere Geometrien und Beanspruchungsbedingungen möglich. Vorsicht ist jedoch geboten, wenn die Dreiachsigkeit des Spannungszustandes größer ist als bei den hier untersuchten Proben. In diesem Falle können die Versagensdehnungen erheblich abnehmen.

Die Anwendung der vorgeschlagenen Dehnungsgrenzen auf ausgewählte strukturmechanische Probleme bei schweren Unfällen zeigt, dass im Vergleich zu den bisherigen Bewertungsmethoden, die noch hinnehmbare Belastung um einen Faktor zwischen 1.25 und etwa 2.0 zunimmt.

Ein ausführlicher Bericht ist unter FZKA 6854 erschienen.

CONTENTS

SUMMARY

A.	OBJECTIVE AND SCOPE	1
B.	WORK PROGRAMME	2
B.1	Definition of test families.....	2
B.2	Tension tests under static load	3
B.3	Bending tests	4
B.4	Tension tests under dynamic load	4
B.5	Tests with curved biaxial specimens under static load	5
B.6	Tests with curved biaxial specimens under dynamic load	5
B.7	Tests with flat biaxial specimens under dynamic load.....	6
B.8	Theoretical investigations using gradient models	6
B.9	Theoretical investigations using stochastic models	6
B.10	Theoretical investigations using local approach models.....	7
B.11	Evaluation of the results and proposal of admissible strains	7
B.12	Sample applications.....	8
C.	WORK PERFORMED AND RESULTS.....	9
C.1	State-of-the-art Report.....	9
C.2	Preparation of the specimens.....	10
C.2.1	Arrangement of the specimens within the given material from the pressure vessel Biblis C.....	10
C.2.2	Material qualification tests	11
C.3	Tension tests under static load	11
C.4	Bending tests	12
C.5	Tension tests under dynamic load	12
C.6	Test with curved biaxial specimens under static load	12
C.7	Tests with curved biaxial specimens under dynamic load	13
C.8	Tests with flat biaxial specimens under dynamic load.....	13
C.9	Determination of the failure strains.....	13
C.9.1	Definition of the local failure strain	13
C.9.2	Methods to determine the local failure strain	14
C.9.2.1	Tension specimens with a hole or with notches	14
C.9.2.2	Circular tension specimens without notches	16
C.9.2.3	Curved biaxial specimens.....	16
C.9.2.4	Flat or curved biaxial specimens without holes under uniform load.....	17
C.9.2.5	Bending specimens with notch	17
C.10	Results for the local failure strains.....	17
C.11	Comments on the accuracy of the local failure strains.....	19
C.12	Theoretical investigations using gradient models	20
C.12.1	Damage enhanced flow theory of gradient plasticity	20
C.12.1.1	Theory.....	20
C.12.1.2	Results and conclusions.....	20
C.12.2	A nonlocal damage model for elastoplastic materials based on gradient plasticity theory	21
C.12.2.1	Theory.....	21
C.12.2.2	Results and conclusions.....	22
C.12.3	Micromorphic deformation and damage model	22
C.12.3.1	Theory.....	22
C.12.3.2	Results and conclusions.....	23

C.13	Theoretical investigations using stochastic models	23
C.13.1	Stochastic material damage model	23
C.13.1.1	Theory.....	23
C.13.1.2	Results and conclusions.....	24
C.13.2	Elastic-plastic behaviour of polycrystalline aggregate with stochastic arrangement of grains.....	24
C.13.2.1	Theory.....	24
C.13.2.2	Results and conclusions.....	24
C.14	Theoretical investigations using local approach models.....	25
C.14.1	Rousselier damage model.....	25
C.14.1.1	Theory.....	25
C.14.1.2	Results and conclusions.....	26
C.14.2	Gradient plasticity theory in combination with a non local damage model	27
C.14.2.1	Theory.....	27
C.14.2.2	Results and conclusions.....	27
C.15	Comparison of the theoretical models.....	28
C.16	Evaluation of the results	29
C.16.1	Size effects.....	29
C.16.2	Prediction confidence curves for the results at room temperature and 400 °C	30
C.16.3	Derivation of a threshold strain	30
C.16.4	Proposal of Limit Strains for Severe Accident Conditions	31
C.16.4.1	Proposal for the specimen shapes and load conditions investigated in the LISSAC project at room temperature and 400 °C.....	31
C.16.4.2	Proposal for the specimen shapes and load conditions at 850 °C	31
C.16.5	Extrapolation of the results to other specimen shapes and load condition.....	32
C.17	Applications	32
C.17.1	Model experiments considering large strains	32
C.17.2	Structural mechanics calculations allowing large strains.	33

CONCLUSIONS

REFERENCES

A. OBJECTIVE AND SCOPE

In last years postulated severe reactor accidents with only a very small probability to occur have been investigated quite extensively. They are expected to cause excessive loads on the reactor pressure vessel. Today advanced structural mechanics codes considering nonlinear geometry and material effects allow rather detailed predictions of the resulting plastic strain fields in the walls of the reactor pressure vessel. However little information is available about plastic strains causing failure. Consequently, reasonable limit strains which should be acceptable under severe accident conditions are lacking, too.

Current rules like the ASME code are mainly stress based concepts and allow only small plastic strains, which is appropriate for design basis accidents. Application of these rules for very unlikely severe accidents, however, would yield over-conservative results. The predicted consequences would include unrealistic severe scenarios.

Therefore in the current project the local failure strains of essential reactor vessel components are investigated. The size influence of the components is of special interest. Typical severe accident conditions including elevated temperatures are considered.

The main part of work consists of test families with specimens under uniaxial and biaxial static and dynamic loads. Within one test family the specimen geometry and the load conditions are similar, the temperature is the same; but the size is varied up to reactor dimensions. Special attention is given to geometries with a hole or a notch causing non-uniform stress and strain distributions typical for reactor components. There are indications that for such non-uniform distributions size effects may be stronger than for uniform distributions. Thus size effects on the failure strains and failure processes can be determined under realistic conditions.

Several tests with nominal identical parameters are planned for small size specimens. In this way some information will be obtained about the scatter. A reduced number of tests is carried out for medium size specimens and only a few tests are carried out for large size specimens to reduce the costs to an acceptable level. For all specimens sufficient material is available from the unused reactor pressure vessel Biblis C. Thus variations of the mechanical material properties, which could impair the interpretation of the test results, can be expected to be quite small. Nevertheless, an adequate number of additional quality assurance tests are planned to check the material homogeneity.

To deepen the understanding of structural degradation and fracture and to allow extrapolations, advanced computational methods including damage models will be developed and validated. The problems to be treated here are quite difficult. Micro-structural effects, for instance, play an important role. Therefore several approaches will be tried in parallel. In some cases so-called non-local concepts, in other cases the description of stochastic properties at the grain size level are considered. Of course, it cannot be expected that all examined models will succeed in describing the experimental findings. Some of the phenomena considered and the related models may turn out to be not really relevant. Some other theoretical investigations are considered to address only special effects and not to yield general predictions.

Based on the results from the present research program and considering the findings in the literature and the experience collected in industry, limit strains will be proposed for severe accident conditions. Using these limit strains – or acceptable strains – a more realistic strain based evaluation concept can be employed for structural mechanics analysis of severe accident consequences. Furthermore the results will help to examine, whether findings from small scale tests can be converted to reactor conditions. It is expected that in this way current over conservatism can be reduced significantly.

B. WORK PROGRAMME

B.1 Definition of test families

As already mentioned, the test families include typical design elements and load cases of a reactor pressure vessel under severe accident condition. An overview of the test families is given in Fig. 1. It starts with the most important family, the flat specimens with a hole at room temperature (RT) under static load (Fig. 1, upper part, left hand side). The ratio between hole diameter and wall thickness is about the same as the ratio between the holes for the control rod drive mechanisms at the reactor vessel head and the wall thickness of this head.

One group of neighbouring families are based on the same specimen shape, but the temperatures are elevated to 400 °C and 850 °C, and dynamic loading is considered (the same symbolic drawing). A temperature of 400 °C may be reached in the upper part of the vessel during a severe accident. Much higher temperatures may be reached in the lower part of the vessel; the value of 850 °C was chosen since it is above the phase change of the material, but on the other hand for this temperature the experimental effort is still acceptable.

Other neighbouring families address variations of the hole in the flat specimens (Fig. 1, upper part, center). The variations include an increased hole, a slot, and notches. To limit the number of tests, the variation of temperature is restricted and only static load is considered.

Neighbouring families are also the bending specimens with a wide notch (half a hole) and a narrow notch (half a slot), (Fig. 1, upper part, right hand side). For these specimens the peak stresses and strains at the notches are intensified in comparison to the tension tests discussed before. Tests are only performed at room temperature under static load.

A bigger step concerning the geometry are the families of circular specimens with notch (Fig. 1, lower part, left hand side). These families are not very typical for a reactor pressure vessel, but they provide some kind of bridge to the standard tension specimens which have also circular shapes. Elevated temperatures and dynamic loading are considered.

Another big step toward real geometry and loading are the families of flat and curved biaxial specimens under static and dynamic load (Fig. 1, lower part). However these tests are rather expensive. To limit the expenses, tests will be done at room temperature, only.

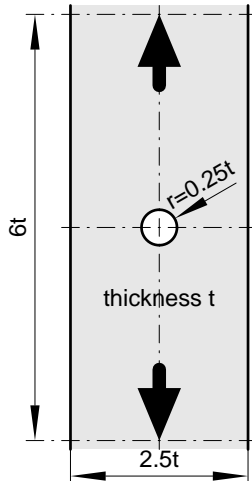
For each of the 24 test families discussed above, the specimen shape is the same, but the specimen size is varied. For the most important test family, the flat specimens with a hole at room temperature under static load, the most extended size variation is considered. The smallest specimen has a thickness of 4 mm, the largest has a thickness of 200 mm which is about the wall thickness of a reactor pressure vessel. For the test families of circular specimens with notch very extended size variations are considered, too; the smallest diameter is 3 mm, the largest 150 mm. More information about size variation chapter B.2 to B.7.

To exclude the interference with other phenomena like variations of the mechanical properties of the material, all specimens are manufactured from the cylindrical section of the unused reactor pressure vessel Biblis C. It consists of the material **22NiMoCr37**. Stress-strain diagrams for this material see Fig. 1a. In addition, the homogeneity of the material will be carefully monitored by a large number of material qualification tests.

FZK will deliver the unshaped specimens, the partners doing the tests are responsible for manufacturing the specimens. There is one exception: VTT performing the biaxial tests with curved specimens under static load will receive the machined specimens from FZK.

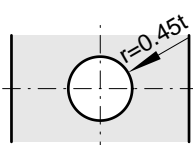
Manufacturing tolerances of the specimens will be given such that the effects on the results can be expected to be in the one-percent region; for the very small specimens this requirement could not always be met. Manufacturing processes for the specimens will be chosen such that surface hardening is minimized in sensitive regions (hole and notch surfaces). Therefore the partners agreed to manufacture the small specimens in the same shop.

B.2 Tension tests under static load



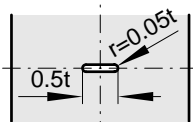
Flat specimen with hole, static load

temperature	thickness t				
	4 mm	20 mm	40 mm	80 mm	200 mm
R.T.	FZK 5	FZK/MPA 2,2(2,3)	FZK/MPA 1	MPA 1	FZK/MPA 1
400°C	EMPA 5(6)	EMPA 2	FZK/MPA 1	MPA 1	
850°C	EMPA 3	EMPA 2		MPA 1	



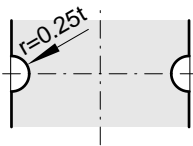
Flat specimen with increased hole, static load

R.T.	FZK 5	FZK 2(3)		MPA 1	
------	----------	-------------	--	----------	--



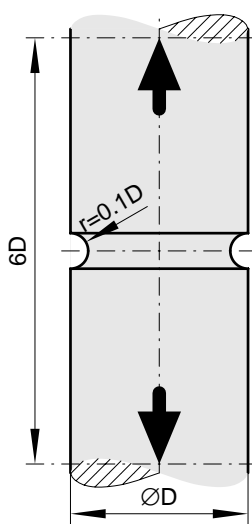
Flat specimen with slot, static load

R.T.	FZK 5(6)	FZK 2(3)		MPA 1	
------	-------------	-------------	--	----------	--



Flat specimen with notches, static load

R.T.	FZK 5(6)	FZK 2(3)		MPA 1	
400°C	EMPA 5(6)	EMPA 2			

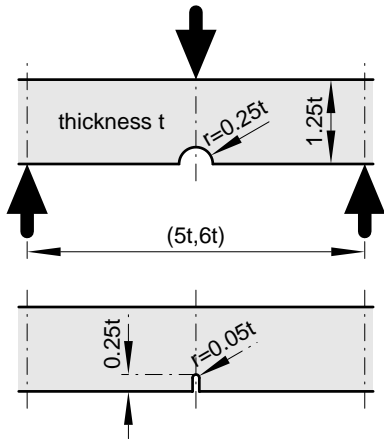


Circular specimen with notch, static load

temperature	diameter D			
	3 mm	9 mm	20 mm	150 mm
R.T.	FZK/JRC 5(5,4)	FZK (4)	MPA 2	MPA 1
400°C	EMPA/JRC 5(6,4)	EMPA (4)	MPA 2	MPA 1
850°C	EMPA/JRC 5(6,3)	EMPA (4)	MPA 2(4)	MPA 1

In this and in the following chapters the digits below the partners performing the tests indicate the number of the planned identical tests. The digits in parentheses indicate the number of tests which have been really carried out.

B.3 Bending tests



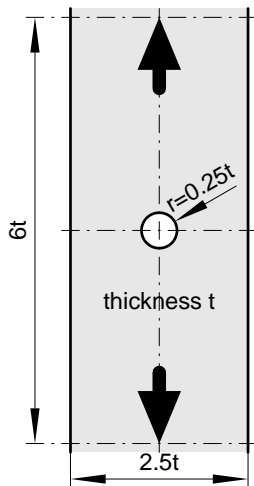
Bending specimen with notch, static load

temperature	thickness t				
	4 mm	20 mm	40 mm	80 mm	200 mm
R.T.	EMPA 5(3)	EMPA 2		EMPA 1	

Bending specimen with narrow notch, static load

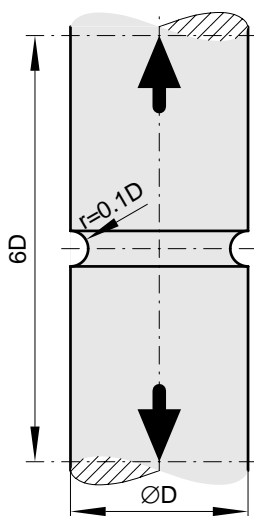
R.T.	EMPA 5(4)	EMPA 2		EMPA 1(2)	
------	--------------	-----------	--	--------------	--

B.4 Tension tests under dynamic load



Flat specimen with hole, dynamic load

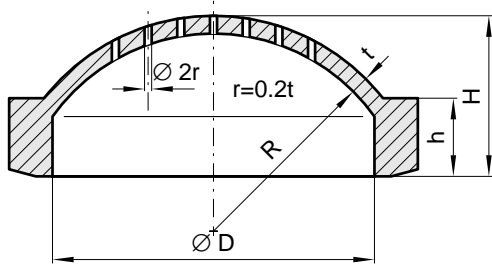
temperature	thickness t				
	4 mm	20 mm	40 mm	80 mm	200 mm
R.T.	JRC 3(4)	JRC 3(2)			
400°C	JRC 3(2)	JRC 3(2)			
850°C	JRC 3	JRC 3(2)			



Circular specimen with notch, dynamic load

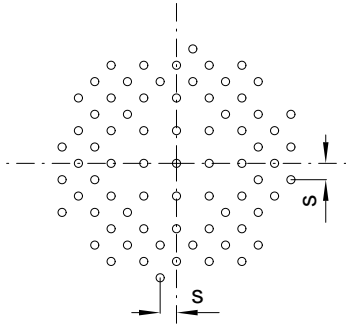
temperature	diameter D			
	3 mm	9 mm	20 mm	150 mm
R.T.	JRC 3(4)		JRC 2	
400°C	JRC 3(4)		JRC 2	
850°C	JRC 3		JRC (2)	

B.5 Tests with curved biaxial specimens under static load



Curved biaxial specimen without hole, static load

temperature	thickness t	
	5 mm	25 mm
R.T.	VTT 3	VTT 1

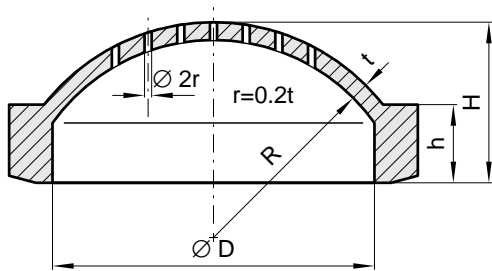


Curved biaxial specimen with holes, static load

R.T.	VTT 3	VTT 1
------	----------	----------

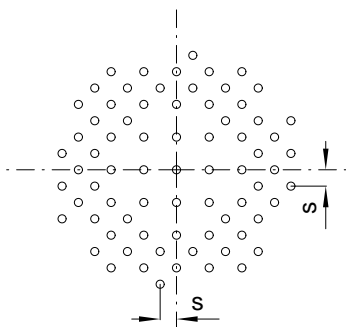
[mm]	R	D	H	h	s
t=5	55.6	90.6	45.2	22	4.6
t=25	278	453	226	110	23

B.6 Tests with curved biaxial specimens under dynamic load



Curved biaxial specimen without hole, dynamic load

temperature	thickness t	
	5 mm	25 mm
R.T.	FZK 3(4)	FZK 2

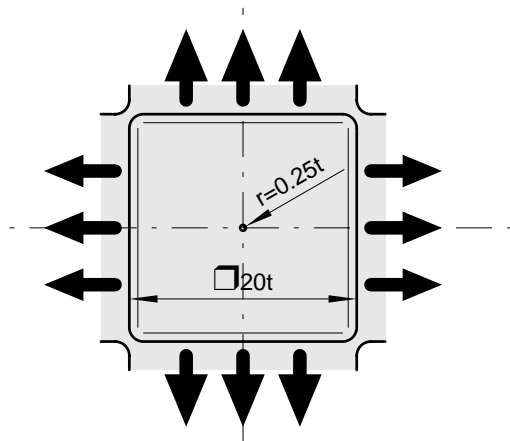


Curved biaxial specimen with holes, dynamic load

R.T.	FZK 3	FZK 2
------	----------	----------

[mm]	R	D	H	h	s
t=5	55.6	90.6	45.2	22	4.6
t=25	278	453	226	110	23

B.7 Tests with flat biaxial specimens under dynamic load



Flat biaxial specimen without hole, dynamic load

temperature	thickness t	
	4 mm	8 mm
R.T.	JRC 2	

Flat biaxial specimen with holes, dynamic load

R.T.	JRC 2	JRC 2(0)
------	----------	-------------

The strain distributions obtained are not equi-biaxial. Displacements are applied with a dynamic test facility only in one direction (in the drawing it is the vertical direction), while displacements are suppressed by an appropriate clamping device in the other direction.

B.8 Theoretical investigations using gradient models

Gradient enriched plasticity and damage models will be examined whether they are able to describe the experimentally observed size effects in deformation and failure. These theories enhance classical models by integral- or gradient-terms of state variables and introduce additional material parameters which can be associated with internal length scales characteristic for the material.

The objective of this theoretical work is the development, analysis and application of such models; this implies an evaluation of their theoretical consistency and an assessment of their qualitative and quantitative properties as well as their ability to interpret experimentally observed size effects.

The following work is planned within LISSAC project:

Employ gradient models for plasticity introduced by Aifantis and co-workers and also by Fleck and co-workers. Furthermore generalize internal variable models (damage) with diffusive transport, analyze the relative importance of gradient terms and calibrate the models in terms of gradient coefficients and associated boundary conditions using solutions of simple loading configurations, parameter calculations and available experimental data on size effects; assess an available numerical scheme to solve non-classical boundary value problems related to the experimental part of the program. Due to the lack of time and material parameters the physical origin of the gradient terms cannot be clarified by using microscopic arguments and macroscopic self-consistent models.

Characterize computationally the ductile failure process using gradient plasticity models and develop a non-local damage model (modified Gurson model). Identify the corresponding material parameters and qualify the models using available experiments.

Develop a thermodynamically consistent plasticity and gradient enhanced damage model (extension of the energy equivalent hypothesis of Sidoroff et al.) for large deformations; identify restrictions on the structure of this gradient damage model within a continuum thermo-mechanics setting.

B.9 Theoretical investigations using stochastic models

Models and methodologies which account for the heterogeneity evolution in plastic flow or damage will be improved or developed in this work package. The failure strains

observed in the experiments including the scatter should be predicted. The results should be used to interpret the experimental findings.

The following work is planned within LISSAC project:

Extend a damage model by evolution equations for higher order statistical moments of the void density. These moments should be treated as spatially correlated. Either the Gurson model or a modified Lemaitre approach should be used. A stochastic term may be added to the flow function to describe the material behaviour. (During the duration of the project it has been realised that this approach was not able to predict the experimental findings and so an interpretation of the experimental results was not possible. The formulation of a slightly more general stochastic model for void nucleation and growth and a comparison with the other models could not be realized due to personal problems.)

Perform a numerical simulation of the stochastic grain structures using the Vornoi tessellation method. Investigate the influence of various stress profiles.

B.10 Theoretical investigations using local approach models

Local approach models in the classical sense use also aspects of the discrete nature of material (Intrinsic length scales such as distance and/or size of inclusions, grain size, etc.) for material characterization. Further, the numerical discretisation (e.g. FEM) is coupled to these intrinsic length scales.

Also more conventional elasto-plastic damage models which are not related to intrinsic length scales (size invariant models) should be utilized to simulate the experiments of the project.

The following work is planned within LISSAC project:

Determine the material parameters of the elastic-plastic Rousselier damage model from tests of small standard laboratory specimens; extend the model to simulate dynamic tests; assess the quality of numerical simulations for differently sized specimens by comparison with experimental results of the project. The visco-plastic material law for the high temperature cases may not be used due to the lack of high temperature material characterisation.

Incorporate a continuum damage model into a general purpose finite element program, determine constitutive parameters using small standard laboratory specimens and use available software; apply the model to other experiments. (In the current project the Gurson-Tvergaard-Needleman model has been used as continuum damage model, but the results achieved were not satisfactory. Therefore the gradient model in cooperation with the Gurson approach developed in B.8 is used for this task.)

Compare the results of the different models with the experiments.

B.11 Evaluation of the results and proposal of admissible strains

Where possible, forces versus characteristic deformations will be measured for all tests performed. These forces divided by the characteristic (smallest) cross sections are defined as nominal stresses. In addition, appropriate post test examinations will be performed to determine the failure strains which is a key issue of the current project.

However, reliable procedures to measure the failure strains during or after the experiments are not available. Therefore the development of such procedures is an essential part of the current project.

Of minor interest are the results for the nominal stresses in the specimens. Here the question is:

What is the size effect on the maximum nominal stress?

More important are the results for the failure strains. The most interesting questions are listed below:

What is the order of magnitude of the failure strain?

What is the size effect on the failure strain?

What is the effect of the specimen shape on the failure strain?

What is the scatter of the results?

What are the failure modes to be expected?

To answer these questions, also findings from theoretical models will be considered. In addition, suitable statistical analyses will be performed.

Based on all these results, it is intended to propose limit strains for severe accident conditions.

B.12 Sample applications

To demonstrate the applicability and the benefit of the results, sample calculations for selected severe accident loads will be presented. It is planned to address the support structure as well as the upper head of the reactor pressure vessel.

C. WORK PERFORMED AND RESULTS

C.1 State-of-the-art Report

It is well established experimentally that for some steels the stress for initiation of yielding decreases with increasing size of the specimens. Even more importantly also the local strains causing failure decrease with increasing specimens, accompanied by scatter. Investigations of such size effects date back to early times of material testing.

A limited review of scaled experiments at room temperature of geometrically similar specimens made of different steels has recently been prepared within the EU-project REVISA [1]. It refers to the size dependence of the initiation of yielding under non-uniform states of deformation and of the plastic deformation and fracture of smooth tensile specimens. Here only two outcomes are mentioned. The experimental studies related to the first issue frequently showed an increase of the yield stress when the size is decreased. Further, the second issue revealed another size effect which indicates an increase of the area reduction after fracture with decreasing specimen size; this has also been found in corresponding experiments of the REVISA project [2] and this latter trend has also been observed recently in tensile tests of sub-size specimens where surface layer effects have been eliminated by electro-polishing [3].

In the domain of micro-plasticity the micro-hardness indentation size effect (increase of hardness with decreasing indenter size) has recently attracted considerable attention [4 – 9]; also the increase of flow stress in plastic deformation with the decrease in size was demonstrated for the micro-bending of thin foil specimens [10].

In brittle or quasi-brittle materials, like concrete, the size effect in fracture is more evident and has been studied intensively [11].

Also for ductile materials sharp notches or cracks (resulting from fatigue or stress corrosion) clearly represent a great danger for fracture and the size dependence of the failure stress, failure strain, and the energy dissipation capability of geometrically similar specimens has been studied (e.g. [12 – 23]). These studies generally demonstrated an increased load carrying capacity and ductility with decreasing size.

However, an increasing number of engineering problems require the determination of failure loads and deformations of structures containing design typical strain concentrators like bore holes, perforations or blunted notches and no sharp notches or cracks. Some testing of geometrically similar specimens of this type but with a relatively small range of sizes has been done, e.g. [24 – 26]. One of the recent contributions was part of the EU project REVISA mentioned above. The results obtained show increased ductility and scatter for the smaller specimens. However, it appears that systematic testing for a variety of specimen shapes and especially over a large range of sizes (geometric scale factor larger than 10 and up to full size conditions) has not been done yet.

It is rather obvious that the various size effects phenomena are related to different micro-mechanical processes and thus different theoretical models should apply. Accordingly, various theoretical attempts have been made or are in a stage of development to account for the observed size effect in material response. It should be mentioned that some of these theoretical concepts originally have been introduced to cope with the "non well posedness" of the more classical material models, which arises when material softening is taken into account. Generally the advanced theories implicate terms which are associated with internal length scales characteristic for the material microstructure. They account in different ways for interactions or heterogeneity over a small but finite material domain on a phenomenological level, still treating the material as a continuum. The interaction between the geometric length of the specimen and the internal length (associated with the underlying microstructure) causes a size-dependent response.

For example, for pre-existing sharp cracks or for sharp notches Linear Elastic Fracture Mechanics or Elastic-Plastic Fracture Mechanics provide a means to capture some size effects; these theories introduce the size dependence via the choice of the fracture criterion without explicitly using an internal material length (instead, a pre-assumed crack length enters into the formulation). To account for size effects in purely plastic deformations, the proposed theories involve internal length scales via integral or gradient terms in the stress-strain relations and/or yield condition (e.g. [1, 27 - 32]). For the treatment of ductile failure and its size dependence a modelling of damage (a usually scalar variable associated to the void fraction) coupled to the stress-strain relations is necessary. Accordingly, the evolution equation for the "damage" internal variable may be enriched by gradient terms accounting for diffusion [33] or may involve integral measures of state variables, for example a (weighted) integral of the local damage variable over a small but finite size material volume (e.g. [26]). Further, some concepts account for the heterogeneity by introducing an "internal length" via the finite element mesh size which is defined by the average distance of inclusions (e.g. [24]). Also size dependence and scatter may be modelled by the introduction of statistical distributions of some material parameter of the constitutive model (e.g. [24]).

Although some of the models involving internal length scales have been matched successfully to a restricted range of experimental results (e.g. [23, 24, 26, 27, 29 - 32]), most of them require essential further developments. This may refer to different aspects: The motivation from micro-mechanics concepts and the embedding in a continuum-thermodynamics framework, the qualitative understanding and trend assessment of the effects of the non-classical terms by utilising the solutions of simple boundary value problems, the numerical solutions with mesh-independent and convergent numerical schemes, the identification of the material parameters - associated with the internal length scales - using suitable experimental results, and testing of their predictive capability by comparison with experimentally observed size effects in deformation and failure on a family of geometrically similar specimens of the same material.

C.2 Preparation of the specimens

C.2.1 Arrangement of the specimens within the given material from the pressure vessel Biblis C

The arrangement of the unshaped specimens for the different test families within the cylindrical section of the pressure vessel Biblis C is shown in Fig. 2. The arrangement is done in such a way that specimens belonging to the same test family are grouped closely together. In this way the inevitable variations, of the material properties of the specimens within one test family are minimized.

The location of the specimens within the wall thickness of the cylindrical section is indicated in the lower part of the figure. As can be seen, the smaller specimens are located in a preferred layer within the wall. Its distance from the outside surface of the vessel is a quarter of the wall thickness. For this layer the material strength is about the same as the mean value of the strength over the wall thickness. (At the outer and inner layer the strength is somewhat higher, at the middle layer it is somewhat lower – quantitative information in the next chapter). Thus also the arrangement of the specimens within the wall thickness of the vessel will help to reduce the effect of variations of the material properties.

In order to control the material homogeneity, a large number of material blocks QA, QB, etc. were reserved. The blocks were cut in slices representing the different layers within the wall thickness. In a last step the slices are cut in pieces which were used to manufacture specimens for standard tension and Charpy impact tests. They will be referred as material qualification tests in contrast to the tests belonging to test families introduced before.

C.2.2 Material qualification tests

To control the material homogeneity, first Charpy impact tests have been carried out which provide integral information about material strength, ductility and dynamic effects. In one series of tests specimens were taken from several blocks all over the relevant segments of the cylindrical section of the reactor pressure vessel, however only from the preferred layer. In this way variations of the mechanical material properties over the cylindrical surface can be studied. Furthermore it was distinguished between specimens in circumferential and axial direction. From the results one can conclude that significant variations over the cylindrical surface do not occur. The directions of the specimens have only small influence.

In another series of tests specimens were taken from only one block, but considering several layers (slices) all over the wall thickness. Thus profiles of the mechanical material behaviour over the wall thickness can be obtained. The results show that the profile is almost uniform. Again the directions of the specimens do not play an essential role.

However the scatter of the results for nominally identical tests is with $\pm 5\%$ rather high and impairs precise statements. Therefore a large number of standard tensile tests have been carried out for many slices of the material blocks. In addition, also many carbon content analyses have been carried out in order to provide some kind of control, since the tensile strength is known to be related to the carbon content.

The results show that the scatter of the material strength is smaller than the scatter obtained by the Charpy impact tests. In the middle of the wall thickness the yield stress is about 6 %, the more important ultimate stress is about 2.5 % lower than at the inner and outer surface. The lowest strength occurs for the blocks QH and QJ. There the yield stress is about 4.5 %, the ultimate stress is about 3 % lower than the mean values.

Thus it can be concluded that the variation of the mechanical material properties is rather low. This is a good basis to investigate the influence of specimen size and shape on the material behaviour.

C.3 Tension tests under static load

Depending on specimen size and temperature quite different testing machines have been used. Figure 3 shows the 100 MN machine for the biggest specimen (MPA, flat specimen, 200 mm thickness). A smaller machine was equipped with an optical measurement system which allows the determination of strain fields at the specimen surfaces using the object grating method (FZK). Figure 4 shows the measuring devices for tests at elevated temperatures (EMPA). In order to reduce oxidation, inert atmosphere was used for the smallest specimens (circular specimens of 3 mm diameter) at 850 °C. For all tests the cross head speed was prescribed such that the mean strain rate related to the gauge lengths of the specimens was about 10^{-3}s^{-1} . In all cases the load versus the increase of the gauge length, in most cases also the load versus the increase (opening) of the hole or the notches have been recorded.

The maximum nominal stresses occurred before fracture. The values are a little bit higher than the corresponding maximum stresses for smooth specimens. This effect is well known. It is due to the higher triaxiality of the stresses in the specimens with holes or notches which hinder necking processes.

During the test of the largest specimen with hole the crack could be seen first inside the hole in the middle of the wall-thickness. With slightly increasing load the crack propagated quickly to the flat surfaces of the specimen. Finally it propagated to the outer contour of the specimen.

Of special interest are the results from the object grating method mentioned above. Here just results for two flat specimens with holes are mentioned. One specimen has a thickness of 4 mm, the other one has a thickness of 20 mm. At the instant when a first crack was observed the hole openings are 75 % and 61 %, respectively. The maximum axial strains at the specimen

surface are 88 % and 73 %, respectively. These results indicate a certain size effect on the deformation at failure. More extensive evaluations and discussions are presented later.

Photographs were taken for many of the broken specimens. Here only a few of them have been selected. Figure 5 shows a typical fracture surface for a flat specimen with hole. Note the normal fracture zone close to the hole where the cracking has started and the shear fracture zone caused during the later phase of the failure process. Figure 6 shows the fracture of circular specimens with notches at room temperature, 400 °C and 850 °C. Note that in parallel to the main crack additional cracks have been initiated which, however, did not propagate very far. (These additional cracks might be one of the reasons why the measured displacements of markings applied in the notches of the big circular specimens led to local failure strains which were unrealistically high).

C.4 Bending tests

The testing machine (EMPA) with a specimen is shown in Fig. 7. In a first set of tests the distance between the support rollers was chosen to be 5 times the specimen thickness; but for the largest specimen the maximum bending force exceeded the capacity of the testing machine. Therefore in a second set of tests the distance between the support rollers was increased to 6 times the specimen thickness.

The cross head speeds were 0.4 mm/min for the small specimens of 4 mm thickness, 1.2 mm/min for the medium size specimens of 20 mm thickness and 2.0 mm/min for the large specimens of 80 mm thickness. The resulting maximum local strain rates turn out to be considerably smaller (factor 5 to 20) than the corresponding strain rates for the tension tests.

For all tests the load versus the increase (opening) of the notch has been measured. For the specimens with wide notches the maximum bending which the facility allowed was not sufficient to initiate a visible crack. Only for the specimens with narrow notches such cracks could be obtained. They occurred at the notch surface in the middle of the specimen thickness. At this instant the test was stopped. There the load-deformation curves had still a slightly positive gradient.

C.5 Tension tests under dynamic load

The dynamic tests are carried out with a modified split Hopkinson bar technique. The principle of this technique (JRC) is shown in Fig. 8. The strain rates which have been realized are between 100 s^{-1} and 400 s^{-1} .

It turns out that at room temperature the stresses versus elongation obtained under dynamic conditions are somewhat higher than under static conditions. This effect is well known. However, for 400 °C the tendency is opposite, which is remarkable. Again, for 850 °C the dynamic stresses are considerably higher than the static stresses.

C.6 Test with curved biaxial specimens under static load

Special facilities had to be designed and manufactured (VTT) for both, the small specimens with a diameter of about 100 mm and the large specimens with a diameter of about 500 mm. A simplified drawing of the facilities is shown in Fig. 9. The load is applied by a liquid with slowly increasing pressure up to a value of about 1200 bar, where failure is expected. During the test the pressure and the resulting vertical displacement are measured.

To make sure that the facility is able to carry the pressure load without excessive deformations causing leakages, quite detailed finite element calculations were performed for the facility for the small specimens as indicated in Fig. 9. The dimensions of the facility for the large specimens were simply obtained by multiplication with the factor five.

The measured displacements of the specimens (increase of the height of the specimens versus pressure yielded very similar curves for the small and large specimens without holes.

A special problem occurred for the specimens with holes. In order to seal these holes, a sealing liner had to be added. Again, the dimensions of the liner for the large specimens are five times the dimensions of the liner for the small specimens. There was only exception. The O-ring for the liner was not scaled up accordingly. Rather the thickness of the O-ring and consequently the size of the nut in the liner for the large specimen was too small in comparison to the liner for the small specimen. Thus the stiffness of the nut region of the liner for the larger specimen was somewhat higher than the stiffness which would have resulted from exact scaling up.

During the tests this small deviation from similarity had a rather significant consequence. The measured displacements of the specimens versus pressure yielded curves which are not similar for the small and large specimens with holes. This finding is an interesting lecture in similarity of structural behaviour. Sometimes very small deviations of the design may result in quite different responses.

Usually failure occurred as a crack with a length on the order of magnitude of the specimen radius. In one case, however, the failure mode was different. Although the pressurizing liquid is almost incompressible, a larger part of the specimen was torn off completely and hurled against the ground. A photograph of this specimen is shown in Fig. 10.

C.7 Tests with curved biaxial specimens under dynamic load

The impact facility VERDY (FZK) was adapted to perform the tests with the small specimens, the impact facility IVAN (FZK) was used for the large specimens, Fig. 11. The specimen is located in the upper part of the facility and the dynamic load is caused by an impact mass of lead accelerated upwards.

The problem was to choose the amount, the shape and the impact velocity of the lead mass in such a way that, limited cracking occurs in the specimens. This could not be achieved for all of the tests. In a few cases no cracking occurred. Consequently for these cases instead of the strain causing failure, a lower strain will be determined where the specimens remain intact.

As an example, Fig. 12 shows the failure of a small specimen with holes as well as the lead mass hitting the specimen.

C.8 Tests with flat biaxial specimens under dynamic load

Biaxial specimens, as shown in Fig. 13, have been constructed. They are of cruciform type, with a finger-like frame holding the central gauge region. Finite element pre-calculations have shown that these specimens produce a fairly uniform strain field, and have a satisfactory behaviour even after yielding. Tests of specimens without and with hole have been performed. The dynamic tensile load is applied along the direction of the Hopkinson bars. The deformation along the transverse direction is constrained to vanish through a special device attached to the specimen and preventing transverse contraction. In the specimen shown, the uniform area is $80 \times 80 \text{ mm}^2$, its thickness is 4mm, and the hole diameter is 2 mm.

Figure 14 shows a failed specimen with hole. It demonstrates that in this case the post test evaluation described in the next chapter was difficult and that the results are assumed to be less accurate than the other results.

C.9 Determination of the failure strains

C.9.1 Definition of the local failure strain

Failure is assumed to occur when a crack has reached a size which is detectable by the methods described later. The further crack propagation is not of interest here, since during this phase the remaining load carrying capacity of structures is not very reliable. It is difficult to predict and may rapidly decrease.

The local failure strain is defined as the maximum true equivalent strain (maximum logarithmic equivalent strain) reached at this instant when a crack is just detectable, however before this crack causes major strain redistributions. Thus in theoretical models describing the strain fields, fracture mechanics approaches with singularities at the crack tip must not be considered.

Usually the local failure strain occurs at the specimen surface (hole or notch surface). It should be mentioned, however, that the crack may be initiated at another position in the interior of the specimen usually with a somewhat smaller equivalent strain but with a higher triaxiality of the stress tensor.

The experiments carried out within the LISSAC project will show that the local failure strain defined above as an equivalent strain (second invariant of the strain tensor) is almost independent of the shape of the specimen. This means, failure is mainly controlled by the equivalent strain. Other quantities characterizing the strain and stress field (other invariants of the strain tensor and the invariants of the stress tensor, for instance) have not a significant influence.

However, it should be pointed out, that for specimens and loads causing other strain and stress distributions than investigated here (higher triaxiality of the stress tensor) this may not be true. This has to be considered in the later chapters where conclusions are made and the applicability of the results is discussed.

C.9.2 Methods to determine the local failure strain

The direct measurement of the local failure strain, i. e. the maximum equivalent strain at the instant when a crack can be just detected, is very difficult. For the LISSAC specimens with holes or notches, for instance, the maximum strain has a quite local character, it occurs at the curved surface of the hole or notch (inside the hole, for instance) and it reaches high values (often more than 100 %). Thus strain gauges can be hardly used. The application of markings and post test measurements of the increased distances between these markings is only possible for large specimens. Even in this case the interpretation of the result is difficult as discussed in chapter C.3. Also the application of a grid at the plane surface of a flat specimen with a hole or notches cannot really yield the maximum strain which occurs at the curved surface of the hole or notch. (But for large specimens the grid could be used to determine the strain distribution close to maximum).

Therefore indirect methods to determine the local failure strain have been developed within the LISSAC project. They are based on post test geometrical measurements at the broken specimens. The aim is to obtain a characteristic deformation δ of the specimen when a crack is just detectable. Then based on this deformation the related strain fields in the specimen can be reconstructed using theoretical models such as finite element models, for instance. The maximum equivalent strain obtained in this way is the local failure strain ϵ .

In the following sub-chapters the different types of LISSAC specimens will be addressed and the appropriate indirect methods to determine the local failure strain will be described.

C.9.2.1 Tension specimens with a hole or with notches

For these specimens used in many LISSAC test families, the so-called “vanishing gap method” will be applied. In Fig. 15 the method is illustrated for a flat specimen with a hole. The broken parts of the specimen are (virtually) moved together such that the gap between the fracture surfaces vanishes. To reach this condition most of the fracture zones of the broken specimen must overlap (Fig. 15c). It is assumed that the configuration obtained in this way represents the shape of the specimen when the crack has started to develop and is just

detectable. The location of this starting crack is the position where the fracture surfaces contact each other.

It is well known that the starting crack will be always perpendicular to the tension stress (normal fracture). Therefore during the search for the position of the starting crack only elements of the fracture surfaces must be considered which are approximately perpendicular to the direction of the tension stress. The relative vertical hole increase, the so-called hole opening at this instant, is defined as the characteristic deformation δ .

This reconstruction would be correct, if during the process of crack propagation the deformed surfaces of the hole did not suffer further shape changes.

The major problem, however, is that in reality the broken parts of the specimens cannot overlap (because two bodies cannot occupy the same space). To overcome this problem the following procedures are applied.

For *tension specimens of medium size* with a wall thickness of 20 mm, for instance, the *vanishing gap method*

using a three-dimensional measuring machine **(1a)**

is applied. Here the geometry of the fracture surfaces of the broken parts of the specimen is scanned by a mechanical probe and the relative hole or notch opening δ is calculated.

For specimens of small size the visual control of the scanning process would not allow sufficient accuracy. Thus for *flat tension specimens of small size* the

vanishing gap method

using optical triangulation **(1b)**

is applied. Different fringe pattern are projected and the resulting pictures of the fracture surfaces are taken by a CCD camera and processed to obtain a three-dimensional image. Using these data the characteristic deformation δ can be calculated.

For *tension specimens of large size* transportation and handling at the measuring machine would be expensive. In this case the

vanishing gap method

inserting plastic material into the gap between the fracture surfaces **(1c)**

turned out to be appropriate. This technique and suitable plastic material is well known in dentistry. The geometry of the resulting mock-up of the gap can be easily measured and again the relative hole or notch opening δ can be calculated.

If the broken parts of circular tension specimen are put together as close as possible, the remaining gap between the fracture surfaces is relatively small. Thus for *small circular tension specimens* the

vanishing gap method

based on direct measurement of the notch opening (1d)

is applied. The small width of the gap between the fracture surfaces is assessed and subtracted for calculation of the relative notch opening δ . For circular specimens often additional cracks can be observed which have not propagated through the whole cross-section (see Fig.6, for instance). The widths of the gaps due to these cracks are assessed and subtracted, too.

As indicated above the relative hole or notch opening δ is used to reconstruct the complete strain fields in the specimen. For each family of tension tests one specimen is selected, the tension force is increased monotonically step by step and finite element calculations are carried out for each step. To describe the material properties the elastic-plastic stress-strain diagrams determined during the material qualification tests are used. Both, the strain fields and the hole or notch opening versus load are obtained. After elimination of the load the strain fields versus the hole or notch opening can be obtained. Thus the strain fields and especially the maximum equivalent strain, which represents the local failure strain, is known for each hole or notch opening δ determined above.

C.9.2.2 Circular tension specimens without notches

These specimens were primarily used to check the material homogeneity and to determine the reference stress-strain-diagrams. Thus these specimens do not belong to any test family. Nevertheless it was tried to determine their local failure strain, too.

For these specimens usually necking before fracture is quite strong, but the necking radius is assumed to be relatively large. In this case the strain fields in the smallest cross section will be relatively uniform and the

cross section reduction method (2)

seems to be suitable to solve the problem. The relative cross section reduction which can be easily measured at the broken specimen represents the characteristic deformation δ .

The radial strain in the smallest cross section is

$$\varepsilon_R = -1 + \sqrt{1 - \delta}$$

and the maximum equivalent strain which represents the failure strain is

$$\varepsilon = \ln \left[1 + \frac{2}{3} \left| \frac{(1 + \varepsilon_R)^3}{(1 - \varepsilon_R)^2} \right| \right] .$$

C.9.2.3 Curved biaxial specimens

For curved biaxial specimens without and with holes the so-called

forging die method (3)

has been developed within a previous research program. A three-dimensional finite element model of the specimen is used as shown in Fig. 16. To reduce the number of elements symmetry conditions are considered and therefore only 1/8 of the shell has been modelled. The measured displacements for selected points of the deformed specimen are used to form the contact surface of a “forging die”. This means, not only one characteristic deformation of the specimen, but several values are considered.

In the deformed specimen cracks should have just started. If in the experiment cracks have already propagated, the measured displacements have to be corrected to describe the earlier state.

Finally the finite element model is pressed against the rigid surface of the forging die, as shown in Fig. 16b. This means, a so-called “contact problem” has to be solved to obtain the related strain fields including the maximum equivalent strain which is the required failure strain.

Sometimes an appropriate correction to describe the state where cracks have just started is difficult. For specimens with holes an additional check is possible by comparing the hole increases measured after the test with the corresponding value obtained from the finite element calculations.

The pressure applied to press the finite element model against the forging die was between 100 and 400 MPa depending on the prescribed displacements (prescribed curvature of the forging die). A pressure increase beyond this value had only negligible influence on the result.

C.9.2.4 Flat or curved biaxial specimens without holes under uniform load.

For these specimens usually the local necking before fracture is relatively small. Therefore the failure strain is about the same as the maximum equivalent strain close to the fracture zone and thus the

thickness reduction method (4)

can be applied. The minimum strain in thickness direction close to the fracture zone which can be easily measured at the broken specimen represents the characteristic deformation δ . Note that this strain is negative. The maximum equivalent strain which is approximately the local failure strain ϵ can be calculated by a simple formula,

$$\epsilon = \ln \left[1 + \frac{2}{3} \sqrt{\frac{1}{1+\delta} - (1+\delta)} \right] .$$

C.9.2.5 Bending specimens with notch

For these specimens

visual inspection during testing (5)

was possible. So the test can be stopped when a crack becomes visible and the relative notch opening, which is defined as the characteristic deformation δ , can be determined directly. Then using this deformation the related strain fields and the maximum equivalent strain can be calculated in a similar same way as described in subchapter C.9.2.1.

C.10 Results for the local failure strains

For most specimens the determination of the characteristic deformation δ and the local failure strain ϵ using the methods discussed before was straight forward. For some specimens the determination of δ and ϵ has been repeated under slightly different conditions or using different methods. Here the most appropriate values have been selected. For the flat biaxial specimens without hole the method to determine the failure strain had to be modified to account for the fact that the dynamic tensile load was applied only in one direction of the specimen while the strain is approximately suppressed in the other direction.

In Figs. 17 to 22 the local failure strains are represented by black symbols versus the radius of the holes or notches of the specimens. Specimens containing no holes or notches

were interpreted as specimens with infinite holes or notches, i.e. $r \rightarrow \infty$. In the diagram the radius $r \rightarrow \infty$ is placed at that position of the abscissa where r would be 100 mm. With this assumption the failure strains for biaxial specimens without holes fit very well with the general trend of the other failure strains.

For some circular specimens of 3 mm diameter it turned out that the manufacturing of the notch was not correct. The depth of the notch varied between 0.300 and 0.332 mm which covers a range of about 10 %. The correct value would have been 0.3 mm. There were also doubts about the surface quality of the notch. Perhaps the cutting tool was defective causing uncontrolled surface hardening. Thus the results should be considered with caution. For a few specimens failure did not occur. Here δ and ϵ are related to the maximum deformation reached and not to failure. For some other specimens which are not members of a test family the values for δ and ϵ have been determined, too. In all these cases the local failure strains are marked by grey symbols.

From the diagrams it turns out that the failure strains are governed by the radius of the holes or notches, while the type of specimen and load has minor influence only. Note that for the biaxial specimens without holes the failure strain does not depend on the specimen size.

In Fig. 17 the somewhat smaller failure strains obtained for bending specimens might be caused by the visual inspection of these specimens during testing. So the crack could possibly be detected at an earlier state than with the vanishing gap methods. This seems to be especially true for the biggest bending specimen where the size of the detectable crack was very small in comparison to the notch radius.

The results obtained from the standard tension tests with smooth specimens (which do not belong to any test family) yield higher failure strains which do not fit with the general trend of the results. Perhaps here the radius should not be assumed to be infinite, rather the radius of the necking before failure or even the radius of the cross section should be taken as the governing parameter.

Comparison of the Figs. 17, 18, 20 and 21 shows that a temperature increase to 400 °C and a change to dynamic load has no significant effect on the failure strain. Thus in these figures the failure strain versus the hole or notch radius can be approximated by the same straight line (straight curve). It has been determined in such a way that the sum of the squares of the deviations from the values obtained for the particular tests is minimized. Here only the values marked by black symbols for finite hole or notch radii (not the values marked by grey symbols and not the values for $r \rightarrow \infty$) were considered.

Of course, the results obtained at 850 °C under static load shown in Fig. 19 and under dynamic load shown in Fig. 22 can hardly be described by the straight line applicable for the specimens at room temperature and at 400 °C. Rather particular straight lines representing the findings in each of the diagrams separately have been introduced. The rules are the same as explained above. However, to improve the poor data basis, for determination of the straight line representing the results at 850 °C under dynamic load, the (somewhat questionable) failure strains for $r = 0.3$ mm described by grey circles have been included.

For 850 °C and static load the failure strain seems to be about the same as for room temperature and 400 °C, if only large notch or hole radii are considered. However the increase of the local failure strain with decreasing radius is much lower than in the cases of room temperature and 400 °C. In other words, for 850 °C and static load there is almost no size effect on the failure strain.

For 850 °C and dynamic load the failure strains are generally higher than discussed before; but again, there is almost no size effect. In fact at 850 °C it has been found that the material under dynamic loading exhibits improved behaviour both in terms of strength and deformation with respect to the static case. As mentioned already, here the data basis is rather poor and therefore conclusions should be made with caution.

C.11 Comments on the accuracy of the local failure strains

As already mentioned, the reconstruction of the strain fields at failure assumes that during the process of crack propagation the deformed surfaces of the hole or notches do not suffer further shape changes. Basic consideration of the stress redistribution caused by a propagating crack (no tension stress normal to the fracture surfaces) support this assumption. In addition, observations made during some of the tests with the optical measurement system indicated that during the process of crack propagation the contour of the holes in the middle of the specimens remains constant. Small changes of the contour which might not be detectable with the optical measurement can be assessed to cause a relative error of the local failure strain of less than $\pm 5\%$.

Another source of errors are lateral displacements sometimes occurring during the crack propagation process. It is assumed that initially when the crack is still small, these lateral displacements are small, too, and can be neglected. Thus, if the broken parts are put together in order to apply the vanishing gap method, lateral displacements are omitted. Nevertheless, uncertainties of the lateral correlation of the broken parts have to be considered. This was especially a problem for the flat tension specimens with 4 mm thickness. Therefore in some cases the lateral correlation was varied allowing lateral displacements up to 3 % of the specimen thickness. The resulting relative errors of the failure strain were up to about $\pm 4\%$. For tension specimens of larger thicknesses or different shapes this error is assumed to be the same.

Measuring errors of axial displacements using the three-dimensional measuring machine have been assessed to ± 0.1 mm. The resulting relative error of the local failure strain is about $\pm 1\%$. Corresponding measuring errors using optical triangulation (small flat tension specimens) or inserting plastic material into the gap between the fracture surfaces (big tension specimens) are assumed to have the same effect on the local failure strain.

However, measuring errors of the axial displacements, using the vanishing gap method with direct measurement of the notch opening, which was applied for the circular tension specimens of 3 mm diameter, have a larger effect on the local failure strain. Here the most difficult problem was to assess the maximum width of the gap between the fracture surfaces and the widths of the possible gaps of other cracks which did not propagate through the hole cross section of the specimens. These gaps had to be subtracted from the measured notch opening. Even with the microscope the resulting error of the notch opening is about ± 0.1 mm. Considering that the initial notch width is only 0.6 mm, which during the test increases to about 1.5 mm, the resulting relative error of the local failure strain is about $\pm 10\%$.

A final source of errors is the reconstruction of the strain fields at failure by finite element calculations. Here uncertainties of the constitutive equations used were discussed. It was concluded that the resulting relative error of the failure strain could be up to $\pm 5\%$.

In order to summarize the particular errors discussed above one has to consider the quadratic error propagation rule. For all the tension specimens – except the circular specimens of 3 mm diameter – the application of the vanishing gap method causes a relative error of the failure strain of about $\pm 8\%$. For the circular specimens of 3 mm diameter the relative error is about $\pm 13\%$.

A more integral check of the accuracy of the vanishing gap method was possible by using the results from the object grating method mentioned in chapter C.3. It was concluded that the above error assessment seems to be reasonable.

The other methods to determine the failure strains were also discussed in some detail. The relative error for the failure strain was assessed to about $\pm 10\%$.

C.12 Theoretical investigations using gradient models

Standard elasticity and plasticity theories, which do not involve an internal length scale in their constitutive equations are not able to describe phenomena like size effects or strain localization. To overcome these problems gradient material models enhance classical models by integral- or gradient-terms of state variables and introduce additional material parameters which can be associated with internal length scales characteristic for the material.

C.12.1 Damage enhanced flow theory of gradient plasticity

C.12.1.1 Theory

In the present work the flow theory of gradient plasticity proposed by Aifantis and co-workers [33-35] is implemented within an element-free Galerkin (EFG) framework. In this gradient theory the usual constitutive relations of classical plasticity are modified by including the Laplacian of the hardening parameter into the standard expression for the yield condition. Material failure (microcrack initiation) can be determined by employing the most common engineering criteria: (a) a local failure strain criterion, (b) a local failure stress criterion, and (c) a local failure damage criterion proposed by Lämmer and Tsakmakis [36].

One of the simplest forms of flow theory of gradient plasticity is based on the gradient modification of the standard expression for the flow stress $\hat{\tau}_{eq} = \kappa(\hat{\gamma})$ to include the Laplacian of the hardening parameter in Eulerian coordinates $\nabla_x^2 \hat{\gamma}$. The corresponding form of the gradient-dependent yield condition reads $f = \hat{\tau}_{eq} - [\kappa(\hat{\gamma}) + c(\hat{\gamma})\nabla_x^2 \hat{\gamma}] = 0$. Then, by including also damage effects, i.e.

$$f = \hat{\tau}_{eq}(1 + X) - [\kappa(\hat{\gamma}) + c(\hat{\gamma})\nabla_x^2 \hat{\gamma}] = 0,$$

a more generalized theory can be developed, where $c(\hat{\gamma})$ is the phenomenological gradient coefficient, which, in general, depends on the hardening parameter $\hat{\gamma}$. Furthermore, the equivalent stress $\hat{\tau}_{eq}$ is the usual von Mises measure defined as $\hat{\tau}_{eq} = \sqrt{3\hat{\boldsymbol{\tau}}' \cdot \hat{\boldsymbol{\tau}}' / 2}$, where $\hat{\boldsymbol{\tau}}'$ denotes the deviatoric part of the Kirchhoff stress tensor $\hat{\boldsymbol{\tau}}$ in the corotational configuration.

C.12.1.2 Results and conclusions

Concerning the deformation behaviour of a simulated cylindrical unnotched specimens, a cylindrical notched specimens and a flat specimens with a central hole, the following conclusions can be drawn from the numerical investigations:

The pre-necking behaviour is not influenced by the specimen size for unnotched tensile specimens due to the absence of strain gradients (Fig. 23).

The pre-necking behaviour is hardly influenced by the specimen size for notched (Fig. 24) and perforated specimens due to the relatively small internal length assumed in conjunction with the small strain gradients (compared to those arisen in the post-necking regime).

The above theoretical predictions are in qualitative agreement with the experimental results obtained in LISSAC. However, concerning the relations between engineering stress and local strain quantities (symmetry cross-section area reduction or notch/hole opening increase), a more pronounced size effect was observed experimentally. The relatively small internal length used in the theoretical analysis could be a possible explanation for this difference. Nevertheless, the pronounced experimental size effect concerns mainly the deformation behaviour of an already cracked material, which is beyond the subject of the present work.

Concerning the failure behaviour, the following conclusions can be drawn from the aforementioned numerical investigations:

When a local failure strain criterion is adopted, then the maximum plastic strain at fracture is not size-dependent for the unnotched specimens, while it decreases with the specimen size for notched or perforated specimens. This size effect is in agreement with the experimental trend.

When a local failure stress criterion is adopted, then the maximum plastic strain at fracture increases with the specimen size for notched or perforated specimens, which is opposite to the experimental trend. For the unnotched specimens, the maximum plastic strain at fracture can decrease or increase with specimen size depending on the critical stress value used.

When a local failure damage criterion $D_c = 0.05$, is adopted smaller specimens have smaller maximum equivalent plastic strains at fracture, which is contrary to the experimental trends observed in LISSAC (Fig. 25-27). This difference is probably due to faster damage evolution in the smaller specimens. In particular, gradient plasticity implies that smaller specimens can sustain higher stress values, which, in collaboration with the stress-controlled damage evolution law, give higher damage rates.

In view of the above remarks, it is concluded that the present gradient plasticity theory can be used to interpret size effects in the deformation behaviour of the material tested in LISSAC. However, concerning size effects in failure, only a local failure strain criterion seems to give convincing predictions. A local failure damage criterion could perhaps give acceptable results if the above framework is modified by adding a plastic potential associated with damage in the yield condition, similarly to the models of Rousselier [37] or Tvergaard and Needleman [38]. Also the inclusion of a damage or strain gradient term in the damage evolution law could possibly solve the problem.

C.12.2 A nonlocal damage model for elastoplastic materials based on gradient plasticity theory

C.12.2.1 Theory

Experimental and theoretical studies have shown that size effects in structure deformations and failure become significant as soon as strain gradients are high in relation to the microstructure. To give an accurate prediction for the failure of structures with high strain gradients these gradients are introduced in the constitutive equations.

In the Gurson Tveergard Needleman (GTN) model [38] one only considers that the material failure process is modelled by nucleation, growth and coalescence of the micro voids. The conventional constitutive relation, which is originally suitable for the macroscopic analysis, is assumed to be valid for the matrix material in microscopic scale.

Due to existence of voids, the strain field of the porous material is inhomogeneous. In the microscopic level the strain concentrates around the voids. According to recent knowledge, the matrix at microscopic level may have significantly different features from that at the macroscopic cases. Discussions about intrinsic material length make it necessary to introduce a material length into constitutive equation of the matrix. From the view point of gradient plasticity the strain variations may significantly change the matrix strength. In this work, we postulate the matrix strength depending on the strain field. The gradient plasticity is introduced into the matrix material to consider the micromechanisms by voids.

In the frame of gradient plasticity, the yield condition is expressed as

$$\Phi(q, p, f, \sigma_y) = \frac{q^2}{\sigma_y^2 \left(\bar{\epsilon}^p, \nabla^2 \bar{\epsilon}^p \right)} + 2q_1 f \cosh \left(\frac{3q_2 p}{2\sigma_y \left(\bar{\epsilon}^p, \nabla^2 \bar{\epsilon}^p \right)} \right) - (1 + q_1^2 f^2) = 0$$

In the equation above the actual stress of matrix, $\sigma_y(\bar{\varepsilon}^p, \nabla^2 \bar{\varepsilon}^p)$, is a function of gradients of plastic strains, represented by $\nabla^2 \bar{\varepsilon}^p$. If material failure is accompanied with high plastic strain gradients, e.g. near a crack tip, the matrix will be strengthened locally to prevent strain localization.

C.12.2.2 Results and conclusions

Due to a rearrangement of partners no results for LISSAC are available. However the model is used by another partner, see chapter C.14.2.1. Based on the new algorithm of gradient plasticity, the formulation and finite element implementation of a micro mechanical damage model by implementing gradient plasticity theory into GTN damage model was done.

C.12.3 Micromorphic deformation and damage model

C.12.3.1 Theory

For describing size effects in **elasticity** constitutive equations for a micromorphic continua are derived:

$$\begin{aligned}\sigma_{ij} &= E_{ijpq} \varepsilon_{pq} + B_{ijpq} \beta_{pq} \\ \tau_{ij} &= A_{ijpq} \beta_{pq} + B_{pqij} \varepsilon_{pq} \\ M_{ijk} &= C_{ijkpqr} K_{pqr}\end{aligned}$$

In these equations, σ is the classical stress tensor, τ is an additional stress tensor depending on the microstructure and M represents the couple stress tensor. ε , β and K are the linearized strain and curvature tensors. In case of isotropy the theory depends on eighteen independent coefficients.

For describing size effects in **plasticity** a micromorphic model with scalar-valued damage is developed. The plasticity theory will be restricted to J_2 -flow. Accordingly, the yield function can be written as

$$f = \frac{1}{1-d} \sqrt{p_1 \sigma^D \cdot \sigma^D + p_2 \sigma^D \cdot (\sigma^D)^T + q \tau^D \cdot \tau^D + r_7 \mathbf{M} \cdot \mathbf{M}} - \frac{k}{1-d}$$

where k denotes the yield stress and d is the variable describing damage effects. σ^D and τ^D are the deviatoric stress tensors, M is the couple stress tensor and p_1, p_2, q, r_7 are material parameters. We set $p_1=1.5$ and $p_2=q=0$. to obtain comparable results with the classical theory. The parameter r_7 is governing the nonlocality in the constitutive behaviour. The parameter k represents the yield stress.

A evolution equation describing ductile damage is given by:

$$\dot{d} = -\alpha_1 \Omega \dot{s}$$

Here, the influence of the triaxiality ratio on the damage evolution is taken into account by Ω .

C.12.3.2 Results and conclusions

The models were programmed and implemented in the finite element code ABAQUS. For plasticity only isotropic hardening is incorporated, while softening in the material response is modelled by using a scalar valued internal variable.

Due to the lack of methods for determining the non classical material parameters the needed constants can not be adapted to LISSAC material. So only the influence of the parameters can be discussed. For the calculations the flat specimen with hole has been modelled in two dimensions assuming plane strain. From the calculations the following results can be achieved:

The micromorphic theories for elasticity are able to predict size effects in dependence of the chosen material parameters. The parameter studies indicate that the results approach asymptotically the classical solution for small values of α (nonsymmetry of the elastic tensor \mathbf{E}) and c_7 (nonlocal elasticity parameter). If c_7 is very large, the results tend asymptotically to a second limit.

The simulations with the micromorphic elastic plastic theory with scalar valued damage predict also size effects. Again the predicted size effect depends on the selection of the used material depending parameters. The parameter is r_7 governing nonlocality in the constitutive behaviour. The effect of parameter r_7 on the distribution of stress σ_y at point 1 as a function of the global strain Δ/l is illustrated in Fig. 28. The maximum stress of all specimen is nearly identical but the failure strain decreases by increasing the specimen's size.

Due to the lack of the LISSAC material parameters a reliable statement if the theory is able to predict the experimentally observed size effect can not be made.

Future works must show if the model is able to predict quantitatively the experimental findings.

C.13 Theoretical investigations using stochastic models

The deformation and failure behaviour of specimens and components is in general not of a deterministic nature. To describe the observed experimental behaviour the statistical scatter should be taken into account. The objective of the LISSAC work package WP7 is to analyse stochastic models for their capability to model size and scatter effects in deformation and failure.

C.13.1 Stochastic material damage model

C.13.1.1 Theory

A Lemaitre continuum damage model (CDM) was modified in a way that the deterministic flow function and consistency condition were replaced by so-called Brown processes. The temporal expected values for the flow function and consistency condition remain so invariably compared with their deterministic counterparts. Due to the non-linearity of the material law however the expected values for the plastic strains and for the damage deviate from the deterministic sizes.

The used flow function Φ including damage and a stochastic term is defined as follows:

$$\Phi = \frac{\sigma_{eq}}{1-f} - r - \sigma_{yield} - \int_0^t \gamma(t') dB_{t'} = 0$$

Here σ_{yield} gives the yield stress and r represents the isotropic hardening of the material. The integral (Ito integral) defines the stochastic disturbance.

C.13.1.2 Results and conclusions

The stochastically extended Lemaitre model has been directly implemented as a material model in a standard FEM program. The size effect evaluations have had to be performed with flat specimens with a hole.

The results for three different sizes are depicted in Fig. 29. To have a pronounced size effect, the stochastic weight has been set to a relatively high value. However, the results do not show a systematic size dependency. Rather the scatter dominates. Adapting the stochastic weight to a more realistic value will even decrease the systematic influence. This will result in a situation, where the large numerical errors induced by the weakening of the convergence

To evaluate the influence of the intentionally introduced stochastic scatter, repeated calculations were done for the middle size (20 mm thickness). The results are summarized in the force/displacement diagram, Fig. 30. The comparison of these results to the results for the different specimen sizes demonstrates the dominating influence of the scatter hiding any systematic size effect.

The essential deficiency of the stochastic approach is that the physical mechanism behind the size effect in failure seems to be of a different nature.

C.13.2 Elastic-plastic behaviour of polycrystalline aggregate with stochastic arrangement of grains

C.13.2.1 Theory

The main idea of the used approach to model elastic plastic behaviour of polycrystalline aggregate was to divide the continuum (e.g., polycrystalline aggregate) into a set of sub-continua – grains. Each grain was simulated as a randomly oriented anisotropic monocrystal. The overall behaviour of the aggregate is then sought through the combined response of the randomly shaped and oriented grains.

The model covers the following main phases of the deformation: (1) elastic deformation; (2) rate-independent plastic deformation (at low temperatures); and (3) potential for generalization towards rate-dependent plasticity (creep) and initialization of microcracks at the inclusions/voids. The analysis was limited to 2D models.

An overview of the constitutive model used to obtain results is described in [39]. The basic idea of the constitutive model is as follows:

The random grain structure (in a plane) is modelled with Voronoi tessellation.

Each grain is assumed to be anisotropically elastic with random orientation of crystal lattice.

Plasticity model assumes plastic deformation by simple shear on the specified set of slip planes. The slip planes are essentially defined by the random orientations of crystal lattice, which differ among the grains.

C.13.2.2 Results and conclusions

The elastic-plastic behaviour of planar polycrystalline aggregates with stochastic arrangement of grains was simulated using a computational approach, which combines the most important mesoscale features and compatibility with conventional continuum mechanics. Polycrystalline aggregates with different number of randomly orientated grains and different boundary conditions were loaded with biaxial loads. From the presented simulations it can be concluded:

Obtained macroscopic strain/stress curves show large scatter, which is decreasing as the number of grains in polycrystalline aggregate increases. Distinctive heterogeneity in plasticity on the mesoscopic (grain size) level can be observed in the stress and strain fields. Local stresses were found to be up to 60% higher than macroscopic stresses. The effect is even more pronounced when dealing with strains, with local strains reaching up to 500% of macroscopic strains. Local stress/strain concentrations due to a grain structure might therefore contribute significantly to localized failure of material and consequently to initiation and growth of microcracks.

Random grain structure might be one of the causes for size effects in polycrystalline aggregates smaller than representative volume element (RVE) size. In this report, the RVE size in elasticity is estimated to be at least 370 grains (Fig. 31), which corresponds to a polycrystalline aggregate size of about $0.5 \text{ mm} \times 0.4 \text{ mm}$. The estimated RVE size in plasticity is at least 800 grains (Fig. 32), which corresponds to a polycrystalline aggregate size of about $0.8 \text{ mm} \times 0.55 \text{ mm}$. These results are in accordance with the literature. Prediction is that RVE size for damage would be $15 \text{ mm} \times 11 \text{ mm}$ in size.

The range of sizes of LISSAC specimens suggests negligible influence of size effects in elasticity and plasticity, which is in accordance with the experimental part of the project. The estimated RVE size for damage however suggests that size effects could be observed within LISSAC experiments. Again, this is in accordance with results of LISSAC tests.

The correlation length is taken as a measure of the grains domain of influence. As long as the macroscopic equivalent stresses are lower than the yield strength, the average grain domain of influence is somewhat larger than the average grain size. With the increase of the load, the average grain domain of influence decreases to about 93% of the average grain size. The correlation length depends on the observed area. Larger search radius is associated with higher correlation length values.

C.14 Theoretical investigations using local approach models

Local approach models in the classical sense use also aspects of the discrete nature of material (Intrinsic length scales such as distance and/or size of inclusions, grain size, etc.) for material characterization. Further, the numerical discretisation (e.g. FEM) is coupled to these intrinsic length scales.

Also more conventional elasto-plastic damage models which are not related to intrinsic length scales (size invariant models) should be utilized to simulate the experiments of the project.

C.14.1 Rousselier damage model

C.14.1.1 Theory

Common material laws for describing ductile deformation like von Mises law can not predict the limits of elasto-plastic deformation. However, in reality, deformation is generally limited by fracture processes. In most metals and alloys second phase particles and inclusions can be observed. If ductile fracture is observed the fracture process can be divided into three phases [40]:

- void nucleation at particles and grain boundaries
- void growth with increasing plastic deformation
- void coalescence \Rightarrow micro crack

The models for describing these phases of ductile fracture are often called damage models or due to their local formulation local approach models. For the calculations done in LISSAC the following models are used:

void initiation:

$$\bar{\sigma}^{VM} \geq R_e$$

void growth (Rousselier model [37]):

$$\Phi = \frac{\bar{\sigma}^{VM}}{1-f} + \sigma_k \cdot D \cdot f \cdot e^{\frac{\sigma^{hyd}}{(1-f) \cdot \sigma_k}} - \sigma_y = 0$$

$f \hat{=}$ void volume

$\sigma_k, D \hat{=}$ material constants

void coalescence [41]:

$$f > f_c$$

For describing size effects an internal length is introduced. In the theoretical framework of the damage models it is assumed that in ductile fracture the crack jumps from void to void. In finite element calculations this can be simulated by finite crack jumps from node to node or from integration point to integration point respectively. Due to this, the absolute size of the finite elements used in the damage calculation must be related very closely to the mean distance of the voids or to the mean distance of the inclusions leading to voids.

For the simulation of the dynamic loaded specimens a damage model is needed which can describe the time depending behaviour. In most cases for metallic materials it can be stated that the stress strain curve is shifted to higher stresses with increasing strain rates [42]. For the simulation of this phenomena a material law have to be found which describes the material hardening in dependence of the strain and the strain rate:

$$\sigma = \sigma(\varepsilon, \dot{\varepsilon}, T)$$

In the LISSAC project only stress strain curves with two different strain rates are available. Due to this, only a relatively simple strain rate dependent material model with few parameters can be chosen. A relatively good approximation for ferritic steels is given by Cowper and Symonds [43]:

$$\sigma^{dyn}(\varepsilon) = \left(\sqrt[p]{\frac{\dot{\varepsilon}_{pl}}{D}} + 1 \right) \cdot \sigma(\varepsilon)$$

Within LISSAC project the Cowper and Symonds law is included in the Rousselier material subroutine to take the dynamic material hardening into account.

C.14.1.2 Results and conclusions

Several finite element calculations show that the Rousselier model is able to simulate the experimental observed load deformation and failure behaviour of the specimen tested in LISSAC with a high accuracy. Examples are given in Fig. 33-35 for the flat tensile specimens with a hole. The model also is able to calculate the initiation and growth of cracks. For all the

calculations the same set of material parameters (stress strain curve and Rousselier parameters) is used.

The model is able to calculate also the location of crack initiation (in the notch ground or close behind for the LISSAC specimens or in the specimen center as observed with the ESIS specimen).

In the deformation behaviour until maximum load the Rousselier model predicts no size effect. A size effect is only predicted near the point of failure (Fig 36). This is in accordance to the experimental observations.

The Rousselier model can predict the influence of the different geometries on the deformation and failure behaviour. The behaviour of the two dimensional loaded head without any holes or notches can also be predicted as for the different specimens with holes and notches.

The fracture strains calculated with the Rousselier model are in good agreement with the experimental ones (Fig. 37). The model also shows, that if the geometry is slightly changed (ESIS geometry) the so called fracture strain differs extremely from the results obtained from the LISSAC specimens. This behaviour is probably a result from the fact that the point of fracture initiation is at the one hand side at or near the surface (LISSAC geometries) or on the other hand in the centre of the specimen (ESIS geometry).

C.14.2 Gradient plasticity theory in combination with a non local damage model

C.14.2.1 Theory

Because the Gurson-Tvergaard damage model [44] initially applied by NRG did not give satisfactory results [45] the non local damage model based on gradient plasticity developed by PSI [46] (see chapter C.12.2) has been applied. The model has been implemented in the finite element program MARC [47].

C.14.2.2 Results and conclusions

The PSI model has been used to perform a finite element calculation for the tensile experiments at ambient temperature with the various sizes of a **round specimen with a notch** (3, 9, 20, and 150 mm diameter). All test specimen have identical geometrical proportions and differ only in size. JRC/ELSA performed also a tensile experiment with 3 mm round specimen with a notch. The specimen JRC/ELSA used has a different geometry compared to the standard geometry used by FZK and MPA.

The experiments showed a size effect with respect to the failure strain (Fig. 38). The calculations predicted a size effect with respect to the failure strain only for the 3 mm specimens (Fig. 39). However, the PSI model predicted the deformation behaviour of the round specimens with a notch reasonably. The nominal stress and failure have been slightly overpredicted. For the small specimens this overprediction is larger than for the larger specimens.

The experiments with the **flat specimens with central hole** (4, 20, 40, 80, and 200 mm thickness) were also simulated numerically. For the calculations plane strain conditions are assumed.

The experiments show a size effect with respect to the failure strains, but no size effect with respect to the ultimate strength (Fig. 40). The calculations predict also a size effect only with respect to the failure strain (Fig. 41). However, this size effect is only apparent for the 4 mm specimen (Fig. 41). For the 4 and 40 mm specimens there is a reasonable agreement between the measured and calculated deformation behaviour. The experiments predict a lower yield point and a lower failure strain. The lower yield point can be explained by the scatter in

the yield stress within the Biblis C vessel. The specimen used for EMPA experiment GR1H, on which the PSI model is based, is taken from a different location than the flat specimens with a central hole. The difference between the measured and predicted failure strain is less than 15%.

The numerical model has also been used to perform finite element calculations for the experiments with the **flat specimens with a double edge notch** (4, 20, and 80 mm thickness). Again plane strain conditions are assumed for the finite element simulations.

The experiments show a size effect with respect to the failure strains, but no size effect with respect to the ultimate strength (Fig. 42). The calculations predict also a size effect, only with respect to the failure strain (Fig. 43). However, this size effect is only apparent for the 4 mm specimen (Fig. 43). The notch opening displacement predicted by the calculations is smaller than the measured notch opening displacement. This is slightly more true for the 4 mm specimen than for the larger specimen. The elongation of the test specimen predicted by the calculations is larger than the measured elongation. Based on the elongation the moment of failure is overestimated for the small specimen and reasonably predicted for the larger specimen. The shape of the stress-strain curves is reasonably predicted until the point of ultimate strength. Beyond that point the experimentally observed decrease of the nominal stress is not well predicted.

C.15 Comparison of the theoretical models

Three different gradient plasticity approaches coupled with damage models were examined and implemented in finite element codes or in an element free Galerkin method. The research works have shown that in principle the gradient plasticity models are able to predict size effects in elasticity, plasticity and damage. However the experimental results show, that a remarkable size effect is only observed in the damage phase that means in the load – deformation behaviour beyond crack initiation.

The gradient plasticity model based on the theories of Aifantis and co-workers is able to describe the load – deformation behaviour of the experiments independent of the used mesh size. However the used damage models are not able to predict the failure strains quantitatively.

The Gurson model extended with a gradient plasticity theory is also able to predict the experimentally observed load deformation behaviour. The model is also independent of the used mesh size. The predicted size effect in failure strains is underestimated especially for the larger specimens.

The model using a micromorphic elasticity or plasticity theory is able to predict size effects in elasticity, plasticity and damage. However a quantitative statement could not be made due to the unknown material parameters could not be determined for the LISSAC material.

In conclusion it can be said that this types of models show a promising way for the element size independent description of size effects. Further investigations have to show if the models can predict the experimentally findings quantitative correct.

The stochastic models take the statistic nature of deformation and failure processes into account. Two in principle different approaches were examined within LISSAC project.

The stochastically extended Lemaitre model is not suitable for predicting size effects because the dominating influence of the scatter is hiding any systematic size effect. This is partly due to some restrictions of the straightforward way of the numerical implementation. However, the essential deficiency of the stochastic approach is that the physical mechanism behind the size effect in failure seems to be of a different nature.

The second approach in the work package models the mesoscopic processes in material deformation. The randomly orientated grains with different shapes were modelled. Now

numerical simulations can predict the influence of the inhomogeneous and anisotropic microstructure on the macroscopic load – deformation and failure behaviour of the material. The simulation can predict to some extent that the microstructure is responsible for the experimentally observed size effect. Until now, the predictions of the model are only of a qualitative nature. To make quantitative correct predictions the model has to be verified and the model parameters have to be refined.

Next local approach models in the classical sense were used. The aspects of the discrete nature of the material (intrinsic length scales such as distance and/or size of inclusions, grain size, etc.) is taken into account by coupling the element size to the microstructure.

The studied Rousselier damage model, included in a commercial finite element code, was able to predict the experimentally observed load – deformation and failure behaviour. The model predicts size and geometry influence on the failure strains quantitatively correct. The numerical results are in good agreement with the experimental findings. A minor disadvantage of this approach is that the mesh size is coupled to the microstructure. Due to this numerical limitations make it difficult to predict the behaviour of very small or very large specimens.

The predictions of the Gurson Tvergaard model did not give satisfactory results. Because of this the Gurson Tvergaard model including gradient terms is used. The results have been already discussed.

In conclusion it can be stated that only the Rousselier model is able to predict the size and geometry effect on the failure strains correct. Nevertheless this model is numerically restricted due to problems resulting from the direct coupling of the element size to the microstructure. A promising way to overcome this limitations could be the coupling of the Rousselier model with probable gradient models.

C.16 Evaluation of the results

C.16.1 Size effects

The experimental results show that for each test family the load deformation curves are approximately size independent up to the point of failure (which, however, may be size dependent). Here the load is defined either as the force acting at the specimen divided by the relevant cross section of the specimen, or as the pressure applied at the specimen. If the maxima of the load deformation curves are reached before failure which is true in most of the cases, also the maximum loads will be approximately size independent.

These findings agree with theoretical studies in chapter C.13.2, considering microstructural phenomena of the material with stochastic arrangements of grains. Based on the long term experience in material testing, the above results are not a big surprise.

The results for the failure strains presented in chapter C.10 are more important. Some of them were not expected at the beginning of the LISSAC project. The findings can be described as follows:

The local failure strains (logarithmic strains) are always higher than 50 %, which is much more than assumed in many analyses, so far.

The local failure strains decrease moderately with increasing specimens, i.e. there is a moderate size effect. For the smallest specimens with thicknesses or diameters of only a few millimetres and hole or notch radii of less than 1mm the local failure strains reach about 150 %, for very large tension specimens typical for a reactor pressure vessel the local failure strains decrease to about 70 %, for large biaxial specimens they decrease to 50 to 60 %.

The parameter which describes the size effect is the radius of holes or notches located in the smallest cross section of the specimens where the stresses reach the highest values. The other dimensions of the specimens play a minor role.

The strong influence of the radius of holes or notches on the local stress and strain is well known since many years. However the influence on the *local failure strain* was not very clear, so far.

The type of specimens and load has only small influence on the failure strain. Tests carried out with tension and bending specimens under uniaxial load, as well as tests with plate or shell type of specimens under biaxial load yield about the same failure strains – provided the hole or notch radius is the same.

This finding was not really expected when the project has been started.

These experimental results can be confirmed by the Rousselier damage model. It was able to predict the experimentally observed size and geometry influence on the failure strains quantitatively correct. The numerical results are in good agreement with the experimental findings.

The obtained scatter is considerable. Nevertheless the essential trends can be clearly seen and – as discussed later – reliable limits can be defined.

Some of these experimental findings about the size effects of failure strains can also be explained qualitatively by the microstructural character of the material with stochastic arrangements of grains, as discussed in chapter C.13.2.

A very interesting experimental result is also obtained concerning the mode of failure. For a test with a curved biaxial specimen under static load provided by an almost incompressible liquid a rather big fragment of the specimen was completely torn off and hurled away.

C.16.2 Prediction confidence curves for the results at room temperature and 400 °C

The results in Figs. 17 to 22 reveal significant scatter. It reflects mainly the intrinsic character of the material. As discussed in chapter C.11, measuring errors may contribute only partly to these deviations.

By using of statistical methods, prediction confidence curves have been determined. Since a temperature increase to 400 °C and a change to dynamic load has no significant effect, all the results shown in the Figs. 17 and 18 as well as in 20 and 21 were considered, except the values for $r \rightarrow \infty$ and the values which are questionable or not applicable for other reasons (values marked by grey symbols). The probability concept used assumes a so-called Student distribution [48, 49] for the failure strain and delivers confidence limits for arbitrary radii as shown in the Fig. 44. The dots describe all the failure strains considered. The straight line represents the mean values of the failure strains as introduced above. The prediction confidence curves below this straight line describe the strains where 2.5 % of the specimens are expected to fail, or 0.5 % are expected to fail, respectively.

From a safety point of view prediction confidence curves would be of interest showing the strains where much less specimens, for instance only 10^{-4} or even 10^{-6} of the specimens are expected to fail. However to obtain such curves just on the basis of statistical evaluations, a huge number of tests would be required – much more than performed within the current LISSAC project.

C.16.3 Derivation of a threshold strain

The distributions of the probability of failure based on the concept of Student, but also the distributions based on other widely used concepts, consider small probabilities of failure

even for strains far away from the mean strains of failure described by the straight lines (curves) in the previous diagrams. However in many cases this assumption might not really reflect the actual physical facts.

Therefore it is interesting to determine the distribution of the frequency of failure directly from the experimental results of LISSAC. This distribution is shown in Fig. 45. It can be interpreted as an approximation of the distribution of the probability of failure for the relevant LISSAC specimens.

Note that these distributions are quite resistant against possible outliers. The character of these distributions may hardly be changed by one or two additional experimental results deviating significantly from the general trend.

Figure 45 shows clearly that the distribution approaches vanishing probability of failure more rapidly than the distributions based on the concept of Student, for instance. This has physical reasons. Failure strains much lower than the mean values may only be caused by large material defects like large inclusions, voids, cracks, etc, or by inadequate heat treatment. However most material defects are excluded by non-destructive material tests performed for the reactor pressure vessel. Consequently the probability of failure for strains much lower than the threshold ϵ_s , marked in Fig. 45 is identical with the probability that large material defects have been overlooked during the non-destructive material testing or that the heat treatment was inadequate. However this probability is rather low, perhaps on the order of 10^{-4} or less.

For the further investigations it is conservatively assumed that the threshold ϵ_s is 40 % below the mean values of the failure strain. The resulting curve (straight line) is also introduced in Fig. 44. For strains below the threshold the probability of failure is governed by the reliability of the non-destructive material tests the heat treatment, etc., as explained above.

C.16.4 Proposal of Limit Strains for Severe Accident Conditions

C.16.4.1 Proposal for the specimen shapes and load conditions investigated in the LISSAC project at room temperature and 400 °C.

Based on the experimental results evaluated above the limit strain versus the hole or notch radius is proposed as shown in Fig. 46. The curve consisting of two straight lines is below the 0.5%-confidence curve and somewhat below the threshold of failure ϵ_s . For a hole or notch radius $r \geq 100$ mm the proposed limit strain is 20 %. For a hole or notch radius $r < 100$ mm the proposed limit strain increases linearly until for $r = 1$ mm it reaches 80 %. For a hole or notch radius $r < 1$ mm a further increase of the limit strain should be considered with caution, since in this region manufacturing problems gain significant influence.

Special attention should be given to the limit strain of 20 % for specimens without holes or notches. In the prediction confidence curves the measured failure strains for these conditions were not included. However a closer view reveals that the failure strains for the smooth specimens varied between 53 % and 62 % (see Figs. 17 and 20) which is much higher than the proposed limit strain. Furthermore it should be considered that all the specimens under discussion here were tested under biaxial load which is rather realistic for the reactor pressure vessel.

If the limit strain is not exceeded, it is suggested that failure should not be considered under severe accident conditions.

C.16.4.2 Proposal for the specimen shapes and load conditions at 850 °C

It may be expected that the scatter is about the same as for room temperature and 400 °C. Thus the limit strains for 850 °C should have the same distance from the mean values of the failure strains (described by the straight lines in Figs. 19 and 22) as in the case of room

temperature and 400 °C just discussed. Note, however, that for 850 °C the data basis is much smaller and consequently also the reliability of the limit strains is smaller than for room temperature and 400 °C.

C.16.5 Extrapolation of the results to other specimen shapes and load condition

As already mentioned in chapter C.9.1, the failure strains obtained and consequently the limit strains proposed are applicable for geometries and load conditions similar to those investigated in the current project. An extrapolation to other conditions should be made with caution.

Theoretical considerations show clearly that for stress distributions approaching uniform triaxiality (the same principle stress in three directions) the failure strains must reduce to very low values given by the volume expansion of the material. By the way, in many theoretical models, including models developed within this project, the volume expansion is restricted to the elastic regime or even neglected.

As a matter of fact, many severe accident conditions of the reactor pressure vessel are addressed by the current research work. But there are exceptions. At the intersection zone between reactor pressure vessel wall and nozzle, for instance, higher triaxiality of the stress conditions may occur than in the tested specimens.

Here two tension tests should be mentioned, recently carried out by MPA within another project, but using specimens made from LISSAC material. The specimens had circular shape, diameter 18 mm, with a circumferential notch like the corresponding LISSAC specimens, notch width 4 mm, notch radius 2 mm, smallest specimen diameter 10 mm. Thus the ratio between the smallest cross section and the cylindrical cross section was 0.31, while for the corresponding LISSAC specimens this ratio was only 0.64. The broken specimens were evaluated in the same way as the LISSAC specimens (vanishing gap method using a three-dimensional measuring machine). The relative notch opening was determined to 24 % and 32 %, respectively; the failure strain was determined to 43 % and 58 %, respectively.

For comparison, the failure strain for the corresponding LISSAC specimens was 114 %. The strong deviation might be caused by the different triaxiality of the stress conditions.

Extrapolation to conditions not too far from the LISSAC test conditions are possible by using theoretical models also developed within the current project. Using the Rousselier model the failure strains for the specimens discussed above were predicted with a high accuracy for room temperature. For higher temperatures no reliable predictions can be made.

However, to get a satisfying basis for such extrapolations and to assess the limits which should not be exceeded, some additional tests with larger variations of the specimen geometry and accompanying analyses with the above models would be helpful.

C.17 Applications

C.17.1 Model experiments considering large strains

Example: Integrity of the reactor vessel head during a postulated in-vessel steam explosion

It is assumed that a steam explosion occurs in the lower plenum of the reactor pressure vessel accelerating a molten core material slug against the upper vessel head. The kinetic energy of the slug which the vessel head can safely carry has to be determined. This complex liquid structure impact problem has been solved by model experiments in scale 1:10 [50].

Figure 47 shows the maximum local strains in mock-ups of the vessel head, obtained for slug impact tests with different impact velocities. In scale 1:10 the impact mass was assumed to be 80 kg. Using this mass the related impact energy can be calculated. It is introduced at the abscissa, too. The different symbols address different test conditions including case A without

upper internal structures, case B with only the upper grid available and case C with all the upper internal structures available. The results are linearly interpolated and extrapolated (in case B the very extended extrapolation is questionable).

According to the state-of-the-art knowledge the acceptable strain is not more than 5 %. Then the admissible liquid slug energy for case A is 0.15 MJ, for case B it is 0.43 MJ and for case C it is 1.04 MJ, as shown in the figure. (In [50] further facts had to be considered and consequently the values mentioned there are a little bit different).

As a result of the current project the acceptable strain is much higher. Using the diagram 3.3.3-1 and considering that the radius of the holes in the (real) head is 50 mm, the acceptable strain is about 28 %. Thus the admissible liquid slug energy increases to 0.3 MJ, 1.07 MJ and 1.33 MJ, respectively.

In other words, using the results of the current project, the admissible energy for case A increases by a factor of 2.0, for case B by a factor of 2.5 and for case C by a factor of about 1.3. (As a consequence of the extended extrapolation, the result for case B is questionable).

Note that simply using the impact energies where in the model experiments the heads fail, would be wrong (too optimistic) for two reasons. In the model experiments the holes in the head are smaller and consequently the failure strain is larger than for the real size head (in diagram 46 compare the failure strains for $r=5$ mm and $r=50$ mm). Furthermore the scatter of failure would not be considered.

The conversion of the admissible impact energies determined in the model experiments into admissible energies for the real size pressure vessel is throughly discussed in [50]

C.17.2 Structural mechanics calculations allowing large strains.

Example: Analysis of the reactor vessel head

The pressure bearing capacity of the upper vessel head has been also investigated using finite element analyses applying both the code ASME III, Division 1, Appendix F 'Rules for evaluation of service loading with level D service limits' [51], as well as the admissible strains determined in the current project. The holes in the upper head have been neglected.

The ASME evaluation has been based on the results of an elastic and an elasto-plastic finite element calculation. For the later case the options for large strains and large displacements have been invoked. The results of the elasto-plastic analysis compared very well with the experimental results obtained by VTT.

The maximum pressure load according to the ASME evaluation of the elastic calculations is 61.56 MPa.

The maximum pressure load according to the ASME evaluation based on the elasto-plastic finite element calculation is 90.85 MPa.

In the current project a limit strain of 20% is proposed at surfaces with a curvature radius $r > 100$ mm. Application of this limit strain results in a maximum pressure load of 116.40 MPa. It should be noted that the ASME evaluations are based on engineering stresses, while the finite element results are given as true stresses and strains. So the limit strain of 20 % from the current project is also interpreted to be an engineering strain which corresponds with a true strain of approximately 18%.

Thus using the admissible strains determined in the current project to calculate the maximum pressure load for the upper head results in an increase by factor 1.28 to 1.89 in comparison to the pressure load according to the ASME evaluations.

Example: Analysis of the reactor vessel support structure

Investigations were performed for a so-called support pad of a reactor pressure vessel of a four loop pressurized water reactor. The finite element discretization of the support pad with a certain section of the pressure vessel wall is shown in Fig. 48. Two cases were considered: Static pressure load at the **top** of the support pad and at the **bottom** of the support pad. Elastic,

plastic and limit analyses were performed using a finite element code and assuming elastic plastic material behaviour at room temperature.

First the results were evaluated according to the ASME code [51], Subsection NB.

The maximum admissible pressure load at the top is

260 ÷ 266 MPa based on elastic-plastic analysis,
280 MPa based on limit analysis.

The maximum admissible pressure load at the bottom is

240 ÷ 256 MPa based on elastic-plastic analysis,
234 MPa based on limit analysis.

Then the results were evaluated using a limit strain of 20 % proposed in the current project at surfaces with a curvature radius $r \geq 100$ mm. Using the diagrams Fig. 49 showing the calculated maximum equivalent strain versus the applied pressure, one obtains

a maximum admissible pressure load at the top of

350 MPa

and a maximum admissible pressure load at the bottom of

333 MPa.

Thus using the results of the current project the admissible pressure loads increase by factor of 1.25 ÷ 1.42 in comparison to the admissible loads by applying the ASME code. This benefit is moderate. If dynamic pressure loads were considered, larger increases could be expected.

CONCLUSIONS

Stresses versus dimensionless deformations are approximately size independent up to failure for specimens of similar geometry under similar load conditions. Also the maximum stress is approximately size independent, if failure occurs after the maximum stress is reached.

Feasible methods could be developed to determine the local failure strains for very different specimens under varying load conditions. The methods are based on post test geometrical measurements of the fracture surfaces allowing a reconstruction of the strain fields using theoretical models. The accuracy of the failure strains obtained in this way could be assessed.

The local failure strains turned out to be more than 50% for large specimens approaching the dimensions of the reactor pressure vessel.

The local failure strains are size dependent. They reach values around 150 % for small specimens with thicknesses or diameters of a few millimetres. See the diagrams Fig. 17 to 22.

The parameter describing the size effect is the radius of holes or notches located in mostly stressed specimen regions. The shape of the specimen and the type of load plays a minor role for the tests performed within the current project.

Some essential findings about size effects can be understood by theoretical studies considering the stochastic microstructural character of the material.

The scatter of the experimental results on structural failure is considerable. However there are indications that the failure strains will hardly fall below a lower threshold.

Thus limit strains depending on the hole or notch radius in the mostly stressed specimen region could be proposed. They are valid for temperatures up to 400 °C. Dynamic loads are included. Refer to the diagram Fig. 46. Limit strains for higher temperatures up to 850 °C may also be proposed, but the reliability is restricted.

The results are also applicable for geometries and load conditions somewhat different from those investigated in the current project. The applicability can be extended by using the recommended theoretical models developed within the current project. However care must be taken when the stress triaxiality increases. In this case the failure strain may decrease significantly.

If in severe accidents the proposed limit strains will not be exceeded, it can be assumed that the structure will not fail.

A remarkable worthmentioning result is, that under excessive load large fragments of structures can be completely torn off to become missiles. This happened during a biaxial test under quasi static load which was provided by (almost incompressible) pressurized oil.

Application of the proposed limit strains to selected severe accident problems showed that the admissible load increases by a factor between 1.25 and about 2.0 in comparison to using state-of-the-art rules.

Severe accident problems causing higher triaxialities of the stress distributions in the reactor pressure vessel seem not to play an essential role. Nevertheless the applicability of the proposed limit strains to such problems is a very interesting question. To answer it, some supplementary tests with specially chosen (and perhaps more sophisticated) specimens leading to higher triaxial stress distributions as well as accompanying calculations are recommended for a future research project.

REFERENCES

- [1] Devos, J., Ritter, B., Auerkari, P., Dupas, P., Malmberg, T., Reactor Vessel Integrity in Severe Accidents, Proc. FISA-97 EU research on severe accidents (Van Goethem, G., Keinhorst, G., Bermego, J.M., Zurita, A. (ed)), Luxembourg, Nov. 17-19, 1997, 113-122, EUR 18258 EN (1998)
- [2] Malmberg, T., Krompholz, K., Solomos, G., Aifantis, E.C., Investigations on Size Effects in Ferritic and Austenitic Materials, Proc. of the 15th Int. Conf. on Structural Mechanics in Reactor Technology (SMiRT-15), paper L06/5, Seoul, Korea, Aug. 15-20, 1999
- [3] Schmitt, W., Stöckl, H., Improvement of micro-mechanical methods considering the size influence especially for the applicability with very small material volumes – clarification of problems of transferability (German), Fraunhofer-Institut für Werkstoffmechanik, Final Report T4/99, Feb. 1999
- [4] Atkinson, M., Origin of size effect in indentation of metals, Int. J. Mech. Sci., 33, no. 10, 843-850, (1991)
- [5] Li, H., Bradt, R.C., The micro-hardness indentation load/size effect in rutile and cassiterite single crystals, J. of Material Sci., 28, 917-926 (1993)
- [6] Stelamshenko, N.A., Walls, M.G., Brown, L.M., Milman, Y.V., Microindentation on W and M₀ oriented single crystals, An STM study, Acta Metall. Mater., 41, no. 10, 2855-2865 (1993)
- [7] Poole, K.J., Ashby, M.F., Fleck, N.A., Micro-hardness of annealed and work-hardened copper poly-crystals, Scripta Materialia, 34, no. 4, 559-564 (1996)
- [8] Jost, A., Bigot, R., Indentation size effect: reality or artefact, J. of Material Sci., 31, 3573-3577 (1996)
- [9] McElhaney, K.W., Vlasak, J.J., Nix, W.D., Determination of indenter tip geometry and indentation contact area for depth-sensing indentation experiments, J. Mater. Res., 13, no. 5, 1300-1306 (1998)
- [10] Stölken, J.S., Evans, A.G., A microbend test method for measuring the plasticity length scale, Acta Mater., 46, no. 14, 5109-5115 (1998)
- [11] Bazant, Z.P., Planas, I., Fracture and size effect in concrete and other quasi-brittle materials, CRC Press LLC (1998)
- [12] Docherty, J.G., Bending tests on geometrically similar notched bar specimen, Engineering , 645-647 (1932)
- [13] Docherty, J.G., Slow bending tests on large notched bars, Engineering, 211-213 (1935)
- [14] Brown, W.F., Lubahn, J.D., Ebert, K.J., Effects of section size on the static notch bar tensile properties of mild steel plate, Welding J., 26, 554s-559s (1947)
- [15] Shearin, P.E., Ruark, A.E., Trinble, R.M., Size effects in steel and other metals from slow notch bend tests, Fracturing of Metals A.S.M., Cleveland, 167-188 (1948)
- [16] Lubahn, J.D., Room temperature crack propagation and size effect on mild steel, Welding J., 34, 518s-528s (1955)
- [17] Wells, A.A., The geometrical size effect in notch brittle fracture, Trans. N. Coast Inst. Eng., Shipbuilding, 71, 278-290 (1955)

- [18] Lubahn, J.D., Yukawa, S., Size effects in slow notch-bend tests of a nickel-molybdenum-vanadium steel, *Proc. Am. Soc. Test. Mater.* 58, 661-677 (1958)
- [19] Wundt, B.M., A unified interpretation of room-temperature strength of notched specimens as influenced by their size, ASME Publication, paper no. 59-MET-9 (1959)
- [20] Yukawa, S., McMullin, J.G., Effects of specimen size and notch acuity on the brittle fracture strength of a heat-treated steel, *Trans. ASME, J. Basic Eng.* 83, 541-544 (1961)
- [21] Kußmaul, K., Roos, E., Doll, W., Zirn, R., Sturm, D., Die Bedeutung von Versuchen mit Proben großer Abmessungen, *Stahl u. Eisen*, 104, no. 18, 913-917 (1984)
- [22] Bazant, Z.P., Size effect in blunt fracture: concrete, rock, metal, *J. Eng. Mech.*, 110, no. 4, 518-535 (1984)
- [23] Bazant, Z.P., Lee, S.-G., Pfeiffers, P.A., Size effect tests and fracture characteristics of aluminium, *Eng. Fract. Mech.*, 26, no. 1, 45-57 (1987)
- [24] Pineau, A., Modelling of scatter and size effects in ductile and brittle fracture, *Proc. of the 14th Int. Conf. on Structural Mechanics in Reactor Technology (SMiRT-14)*, Plenary lecture 4, Lyon, France, Aug. 17-22, 1997
- [25] Marini, B., Carasson, S., Wident, P., Soulat, P., Evaluation of the fracture toughness of a C-MN steel using small notched tensile specimens, in: *Small Specimen Test Techniques*, (Corvin, W.R., Rosinski, S.T., van Walle, E. (ed.)), ASTM STP 1329, 513-522 (1998)
- [26] Giovanola, J.H., Kirkpatrick, S.W., Using the local approach to evaluate scaling effects in ductile fracture, *Int. J. of Fracture*, 92, 101-116 (1998)
- [27] Nix, W.D., Gao, H., Indentation size effects in crystalline materials: a law for strain gradient plasticity, *J. Mech. Phys. Sol.* 46, no. 3, 411-425 (1998)
- [28] Gao, H., Huang, Y., Nix, W.D., Hutchinson, J.W., Mechanism-based strain gradient plasticity, I. Theory, *J. Mech. Phys. Sol.*, 47, 1239-1263 (1999)
- [29] Aifantis, E.C., Higher order gradients and size effects, in: *Size-Scale Effects in the Failure Mechanisms of Materials and Structures* (Carpinteri, A. (ed.)), E & FN Spon, London, 231-242 (1996)
- [30] Zhu, H.T., Zbib, H.M., Aifantis, E.C., Strain gradients and continuum modelling of size effect in metal matrix composites, *Acta Mech.* 121, 165-176 (1997)
- [31] Tsagrakis, I., Malmberg, T., Aifantis, E.C., Gradient Plasticity and Size Effects, *Proc. 5th National Congress on Mechanics*, Ioamina, Greece, Aug. 1998, 953-960 (1998)
- [32] Aifantis, E.C., Strain Gradient Interpretation of Size Effects, *Int. J. of Fracture*, 95, 299-314 (1999)
- [33] Aifantis, E.C., On the role of gradients in the localisation of deformation and fracture, *Int. J. Eng. Sci.* 30, 1279-1299 (1992)
- [34] Aifantis, E.C., The physics of plastic deformation, *Int. J. Plasticity*, 3, 211-247 (1987)
- [35] Aifantis, E.C., Gradient plasticity, in: *Handbook of Materials Behavior Models*, (J. Lemaitre, ed.), Academic Press, New York, 281-297 (2001)

- [36] Lämmer, H., Tsakmakis, Ch., Discussion of coupled elastoplasticity and damage constitutive equations for small and finite deformations, *International Journal of Plasticity*, 16, 495-523 (2000).
- [37] Rousselier, G., Ductile Fracture Models and their Potential in Local Approach of Fracture, *Nuclear Engineering and Design* 105, S. 97/111 (1987)
- [38] Needleman, A., Tvergaard, V., An Analysis of Ductile Rupture in Notched Bars, *J. Mech. Phys. Solids* 32, pp. 461-490 (1984)
- [39] Cizelj, L., Kovac, M., Constitutive Models for the Elastic-Plastic Polycrystalline Aggregate with Stochastic Arrangements of Grains, Revision 0, Ljubljana, Institut Jozef Stefan, 2001, IJS-DP-8334
- [40] Stroppe, H., Ermittlung der Bruchzähigkeit duktiler Werkstoffe aus Parametern der Mikrostruktur und der Fließkurve, *Neue Hütte*, 26. Jahrgang, Heft 12, pp. 446-448 (1981)
- [41] Seidenfuss, M., Untersuchungen zur Beschreibung des Versagenverhaltens mit Hilfe von Schädigungsmodellen am Beispiel des Werkstoffes 20 MnMoNi55, Dissertation, Universität Stuttgart (1992)
- [42] Demler, T., Untersuchungen zum Einfluss der Beanspruchungsgeschwindigkeit auf das Festigkeits- und Zähigkeitsverhalten von Feinkornbaustählen, Dissertation Universität Stuttgart (1990)
- [43] Cowper, G.R., Symonds, P.S., Strain Hardening and Strain Rate Effects in the Impact Loading of Centilever Beams, *Techn. Report No. 28, Contract No. 562(10)*, Brown University, Providence, RI (1957)
- [44] Church, J.M., LISSAC - Review of the Gurson-Tvergaard Model of Ductile Damage Accumulation, NRG report 20292/01.38931/P (2001)
- [45] de Groot, S., Church, J.M., LISSAC - Study on the implementation of the Gurson-Tvergaard damage model in Finite Element code MARC, NRG report 20292/02.46866/C (2002)
- [46] Chen, J., Yuan, H., Kalkhof, D., A Nonlocal Damage Model for Elastoplastic Materials based on Gradient Plasticity Theory, *PSI Bericht Nr. 01-13, ISSN 1019-0643* (2001)
- [47] MARC User's Manuals, MSC Software Corporation, MSC. Marc-Version 2001
- [48] Student, The Probable Error of a Mean, *Biometrika*, 6, 1-25 (1908).
- [49] Fisher, R. A., *Statistical Methods for Research Workers*, 10th ed. Edinburgh: Oliver and Boyd (1948).
- [50] Krieg, R., Dolensky, B. Göller, B., Hailfinger, G., Jordan, T., Messemer, G., Prothmann, N., Stratmanns, E., Load carrying capacity of a reactor vessel head under molten core slug impact., *Nucl. Eng. and Design*, 2813 1-17 (2003)
- [51] ASME Boiler and Pressure Vessel Code, Edition 1998 plus Addenda up to 2000, Section III, Div. 1

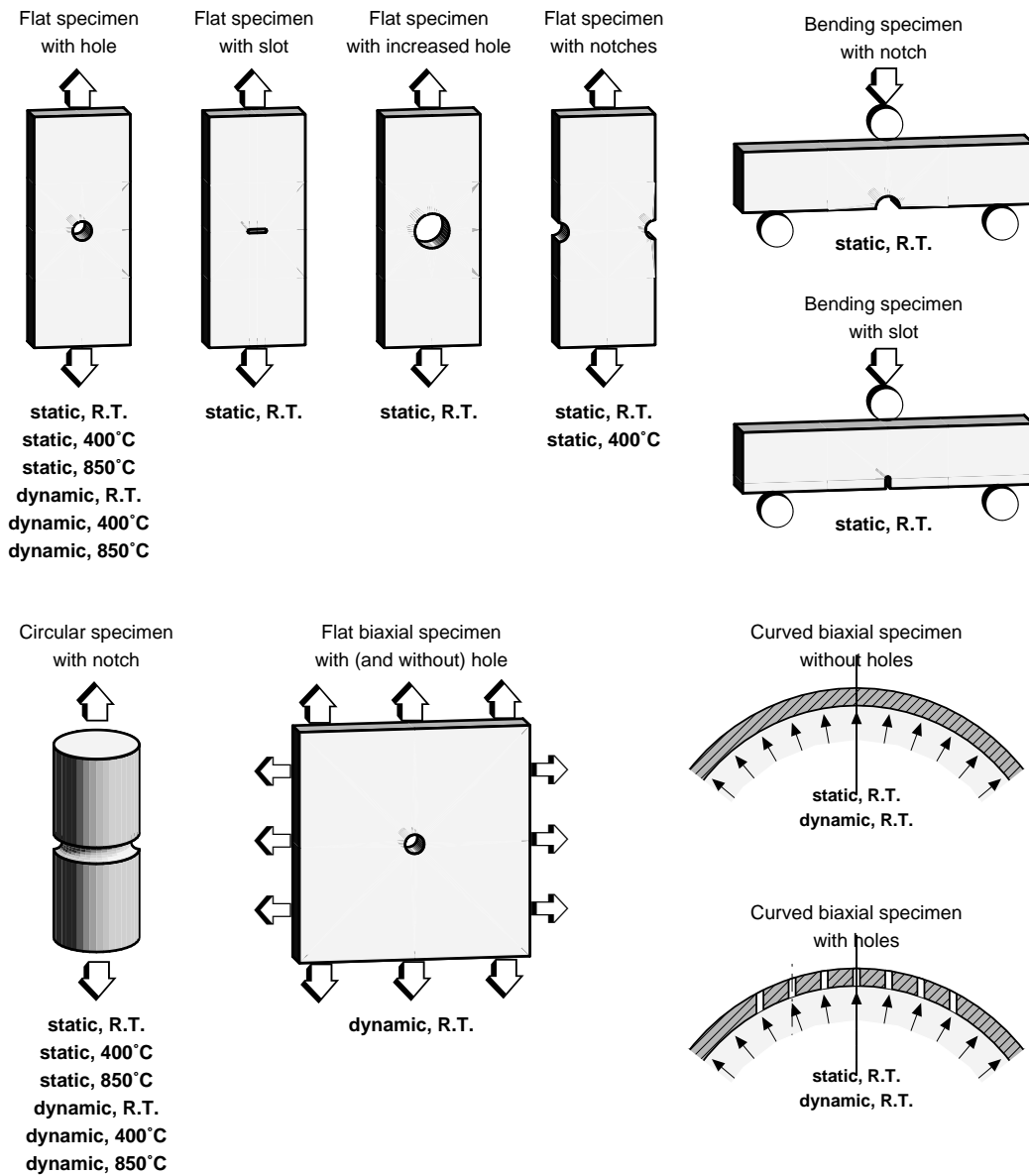


Fig. 1: Overview of the test families

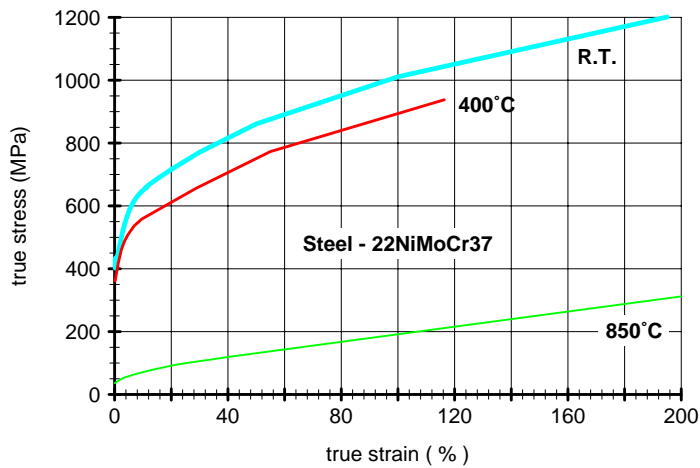
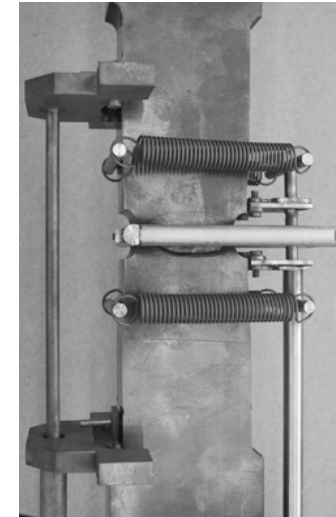


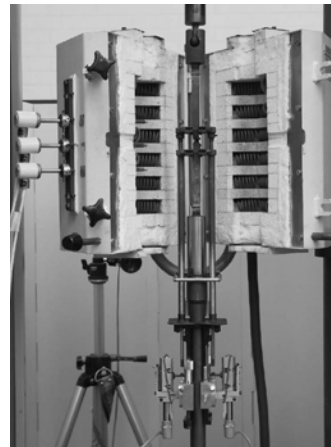
Fig. 1a: Stress-strain diagrams for the material used



Fig. 3: Tensile testing machine of 100 MN (MPA) used for the flat specimen of 200 mm wall thickness



Deformation measurement on flat specimens of 20 mm wall thickness



Heating facility and measurement on flat specimens of 4 mm wall thickness at 850 °C

Fig. 4: Measuring devices (EMPA) for tests at elevated temperature

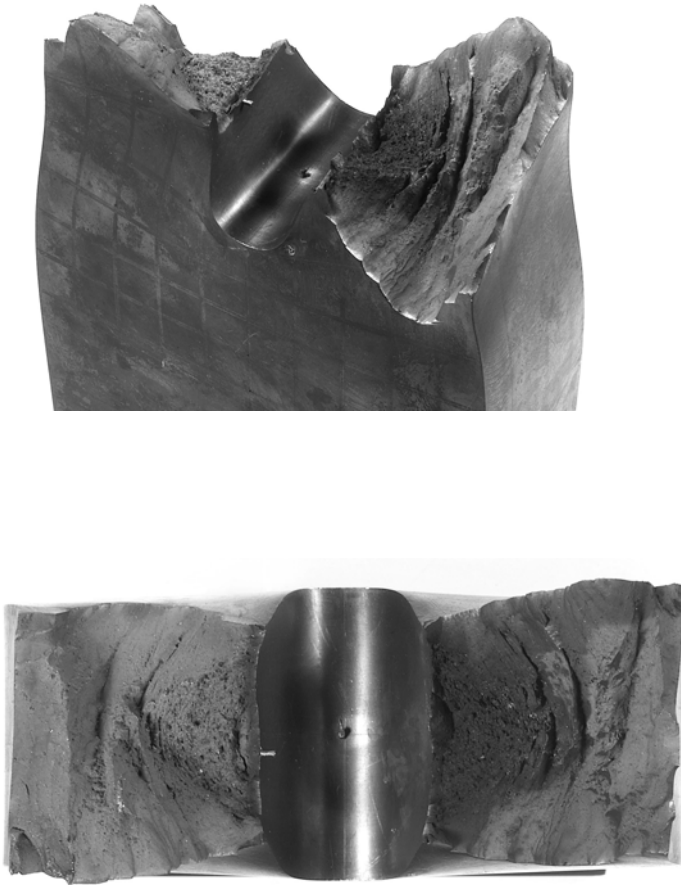


Fig. 5: Fracture surface for a flat specimen with hole, 80 mm wall thickness, tested at 400 °C

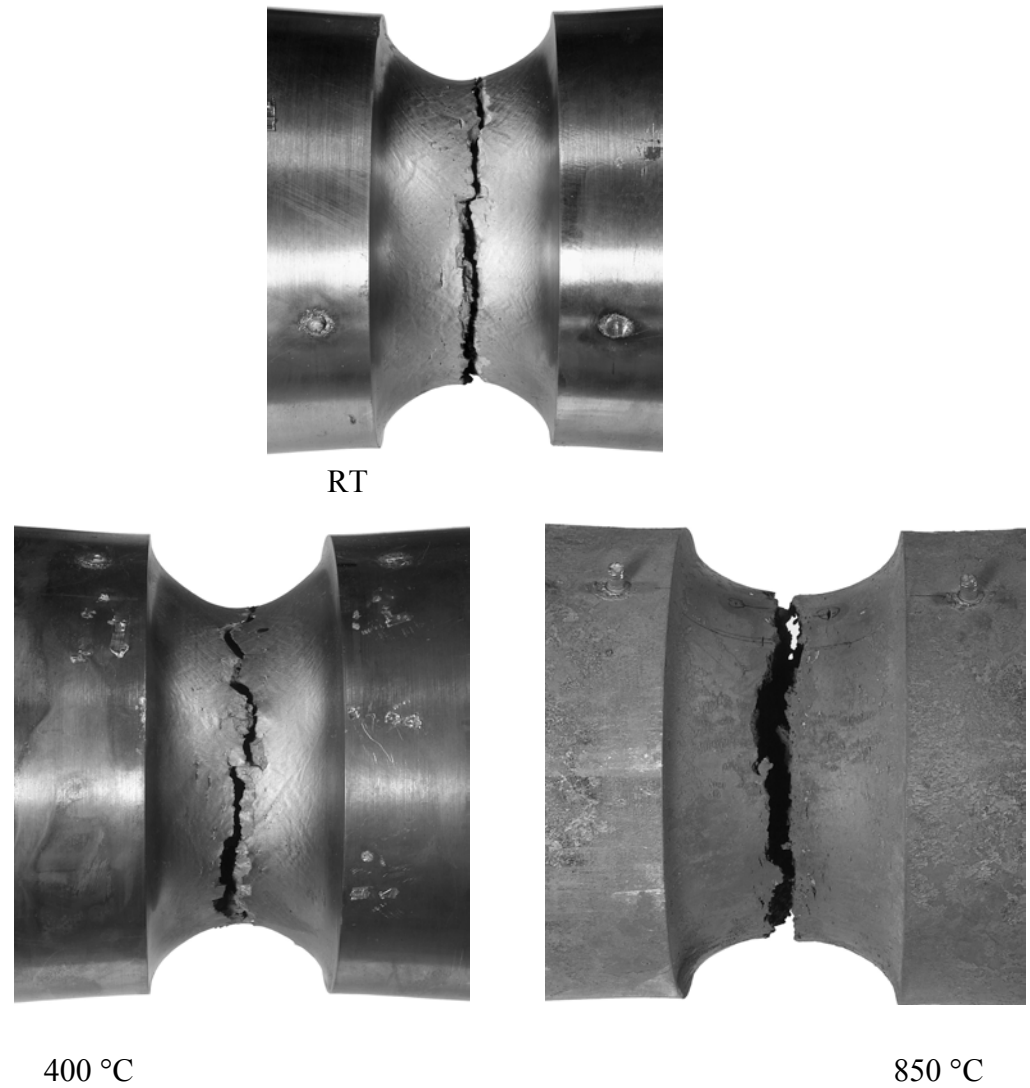


Fig. 6: Fracture of circular specimens of 150 mm diameter tested at different temperatures

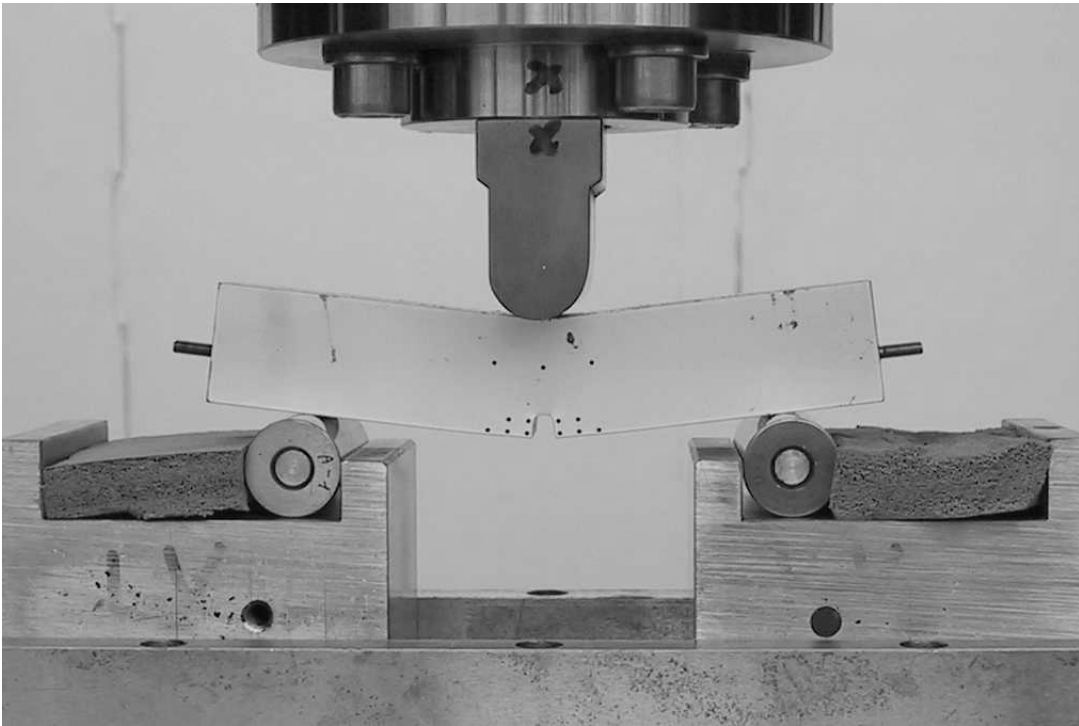


Fig. 7: Testing machine (EMPA) with a bending specimen

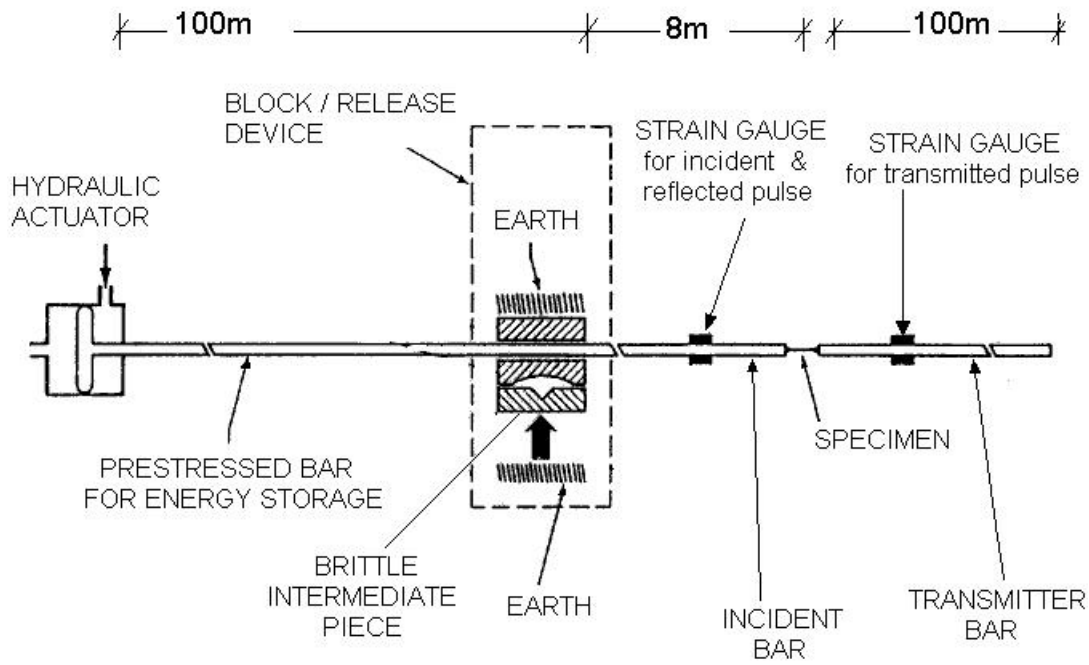


Fig. 8: Principle of functioning and dimensions of the large Hopkinson bar at the Large Dynamic Test Facility (LDTF) of the JRC-Ispra

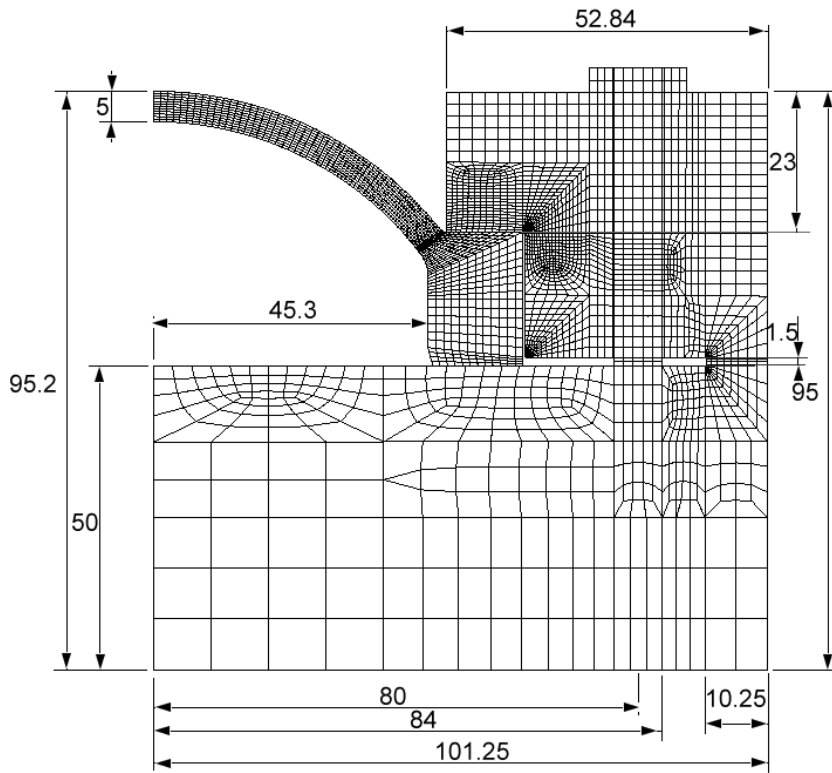


Fig. 9: Finite element model for analysis of the test facility

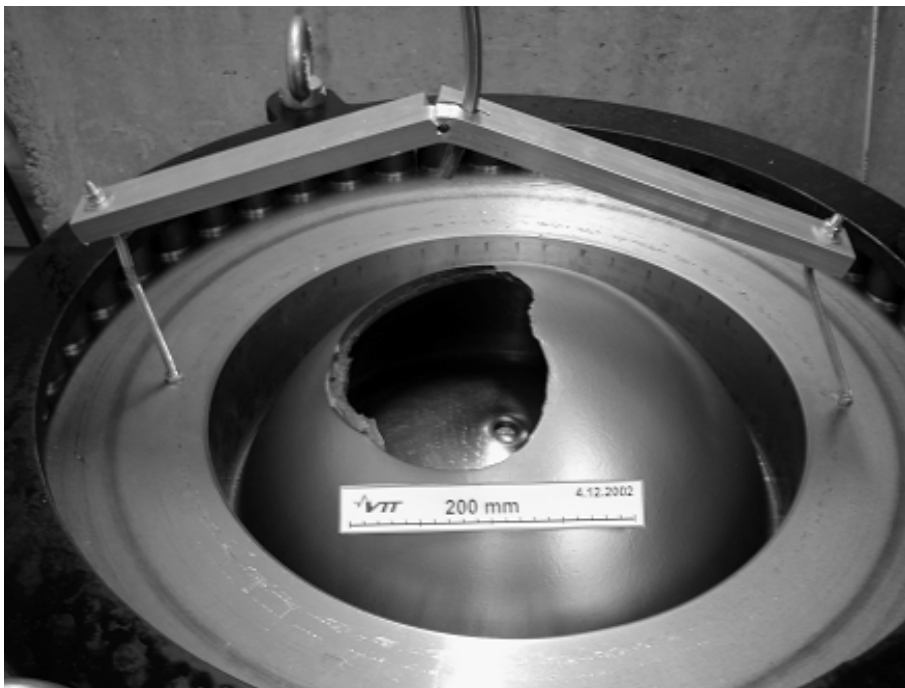


Fig. 10: Failure of one of the large specimens.
A large part of the specimen was completely teared off.

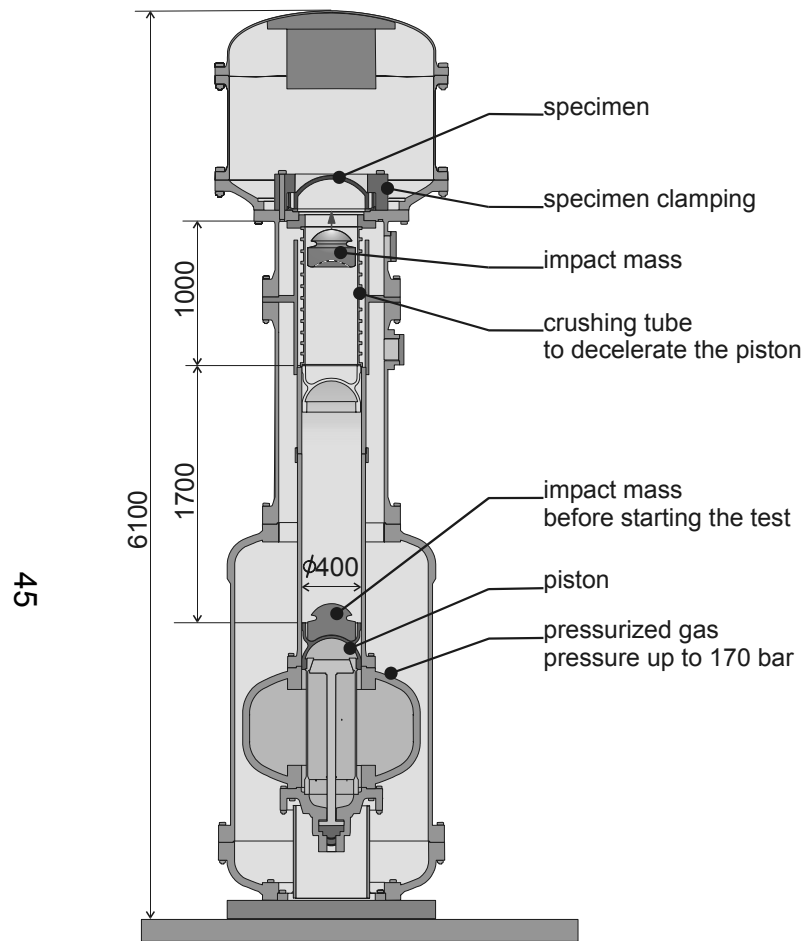


Fig. 11: Impact facility IVAN for the tests before and after the impact



Fig. 12: Failure of a small specimen with holes and lead mass with the large specimens

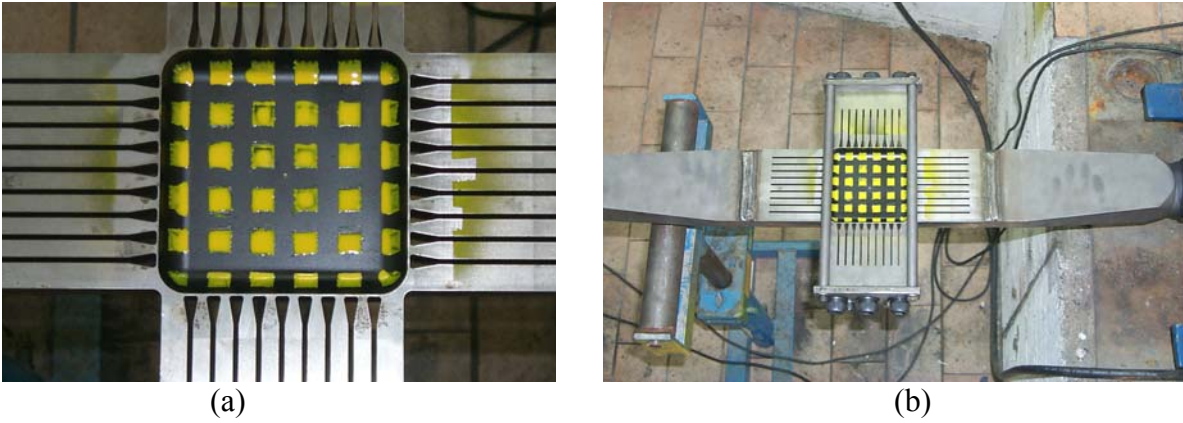
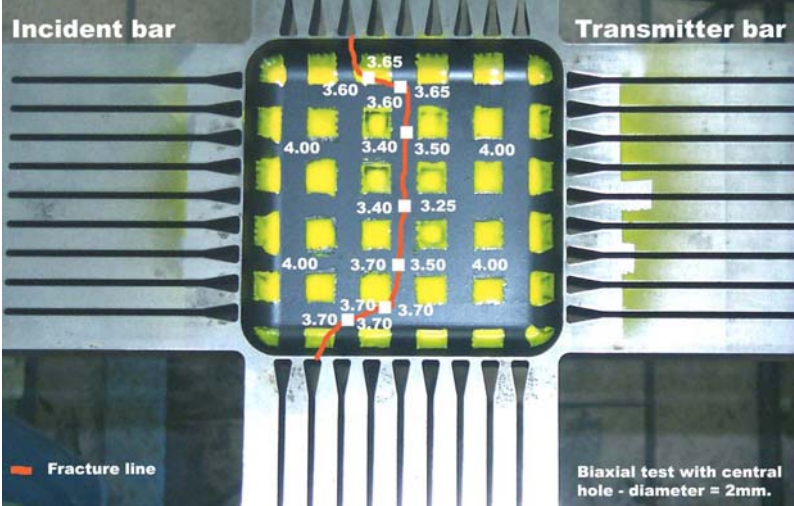


Fig. 13: (a) Details of gauge area of flat biaxial specimen with hole;
 (b) Specimen with holding arms and device for preventing transverse contraction



as seen below, fracture goes through the central hole



Fig. 14: Specimen EO with hole before and after the test

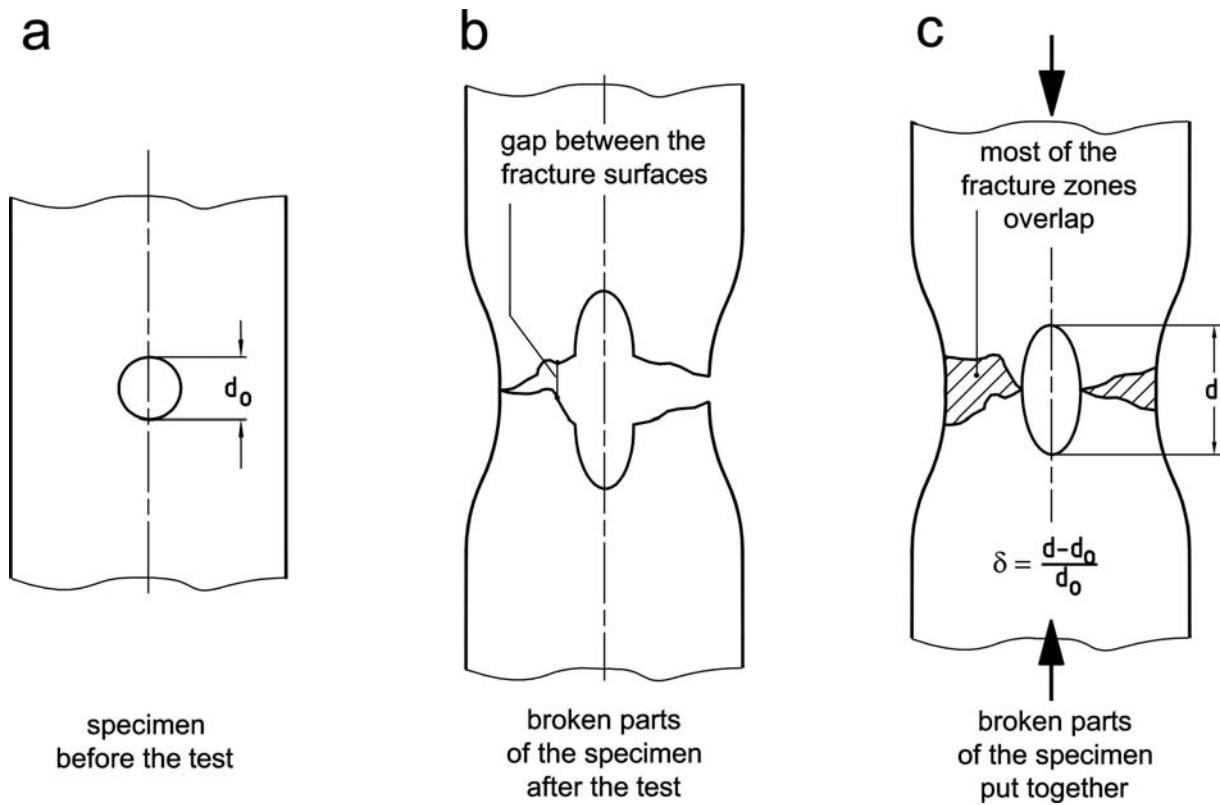


Fig. 15: Principle of the vanishing gap method

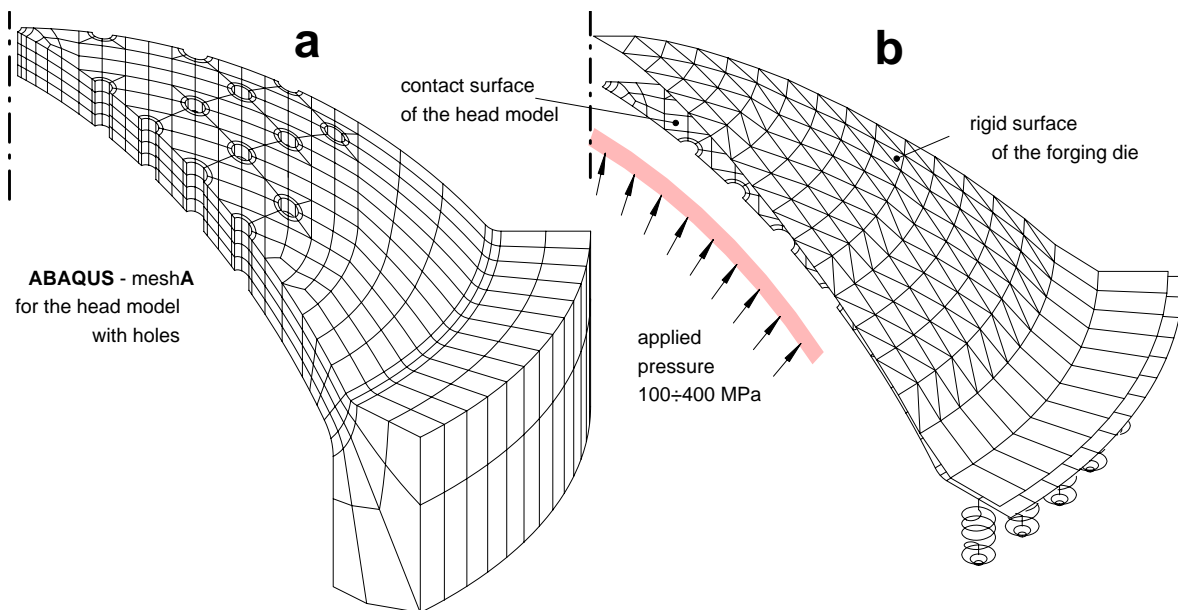


Fig. 16: Determination of the strain distribution using the forging die method.

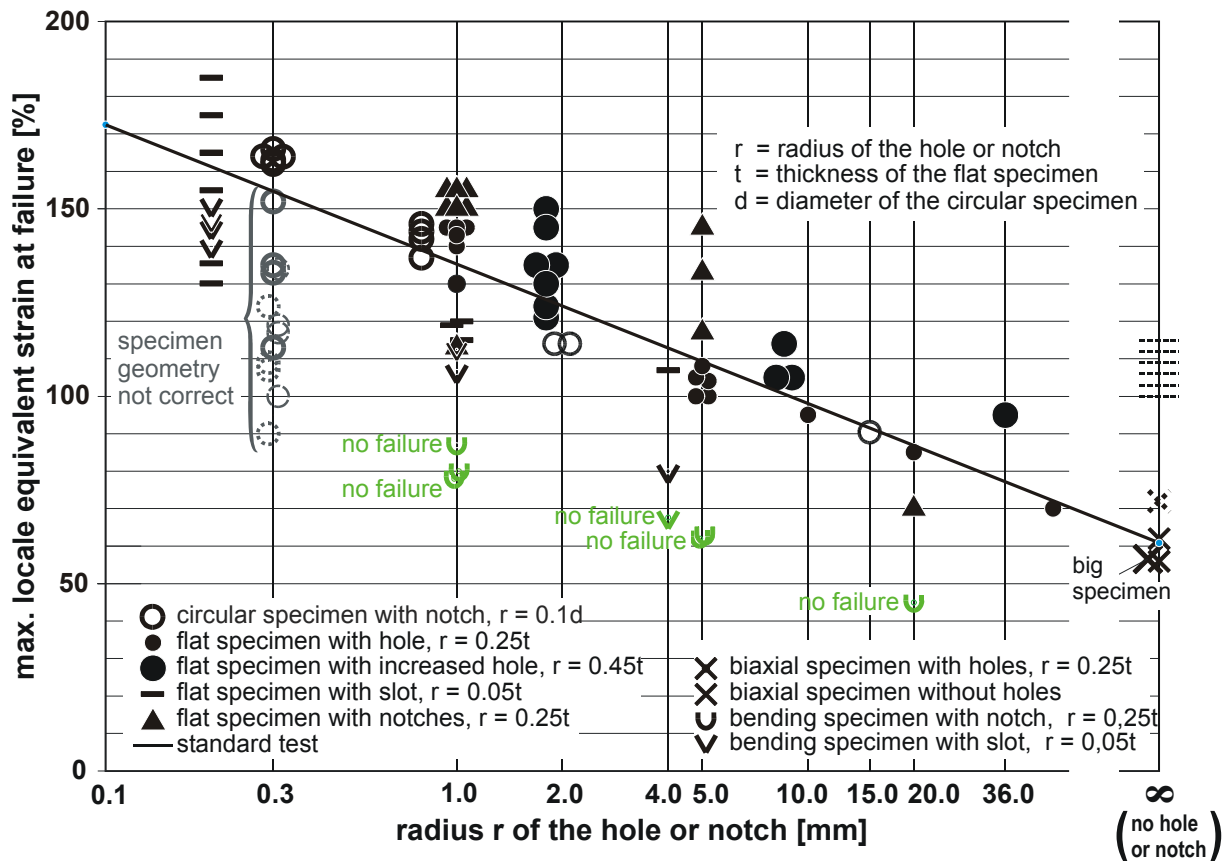


Fig. 17: Main results of LISSAC for RPV material at room temperature, static tests

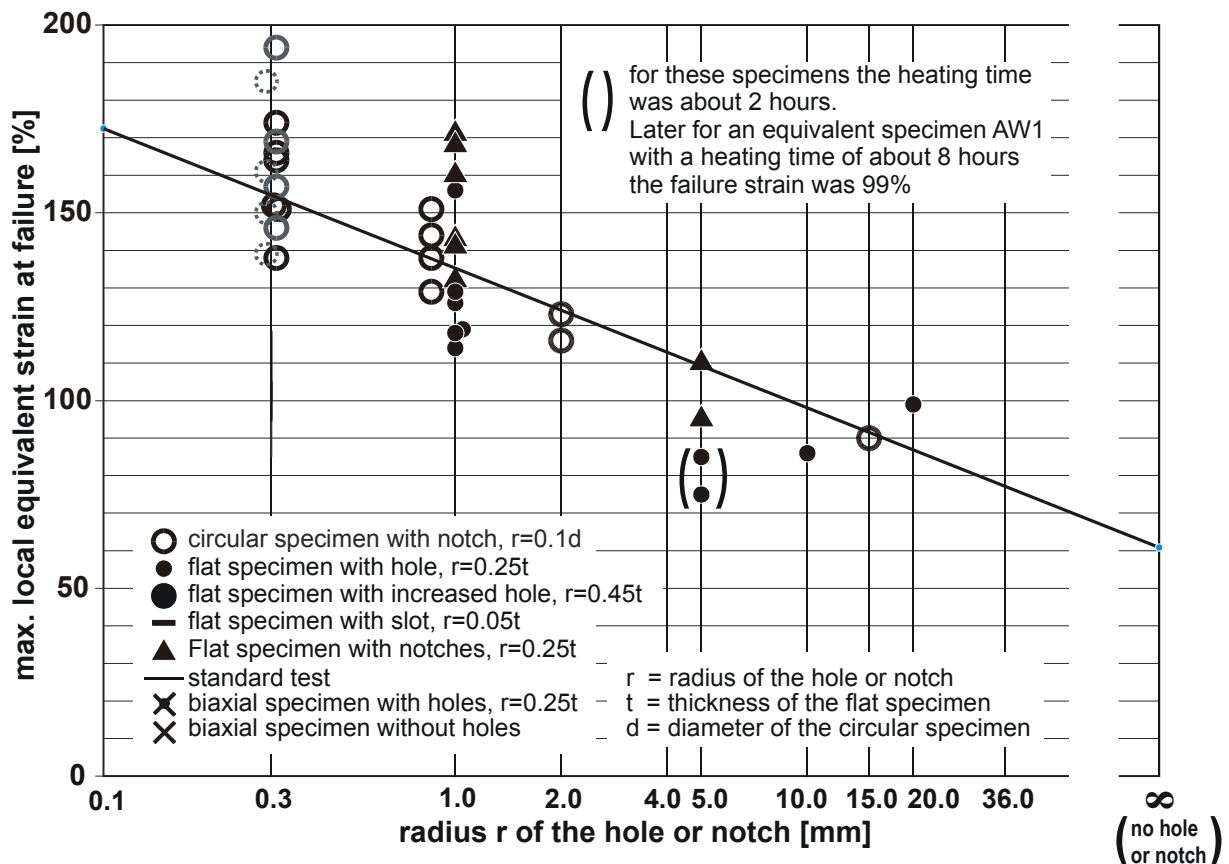


Fig. 18: Main results of LISSAC for RPV material at 400 °C, static load

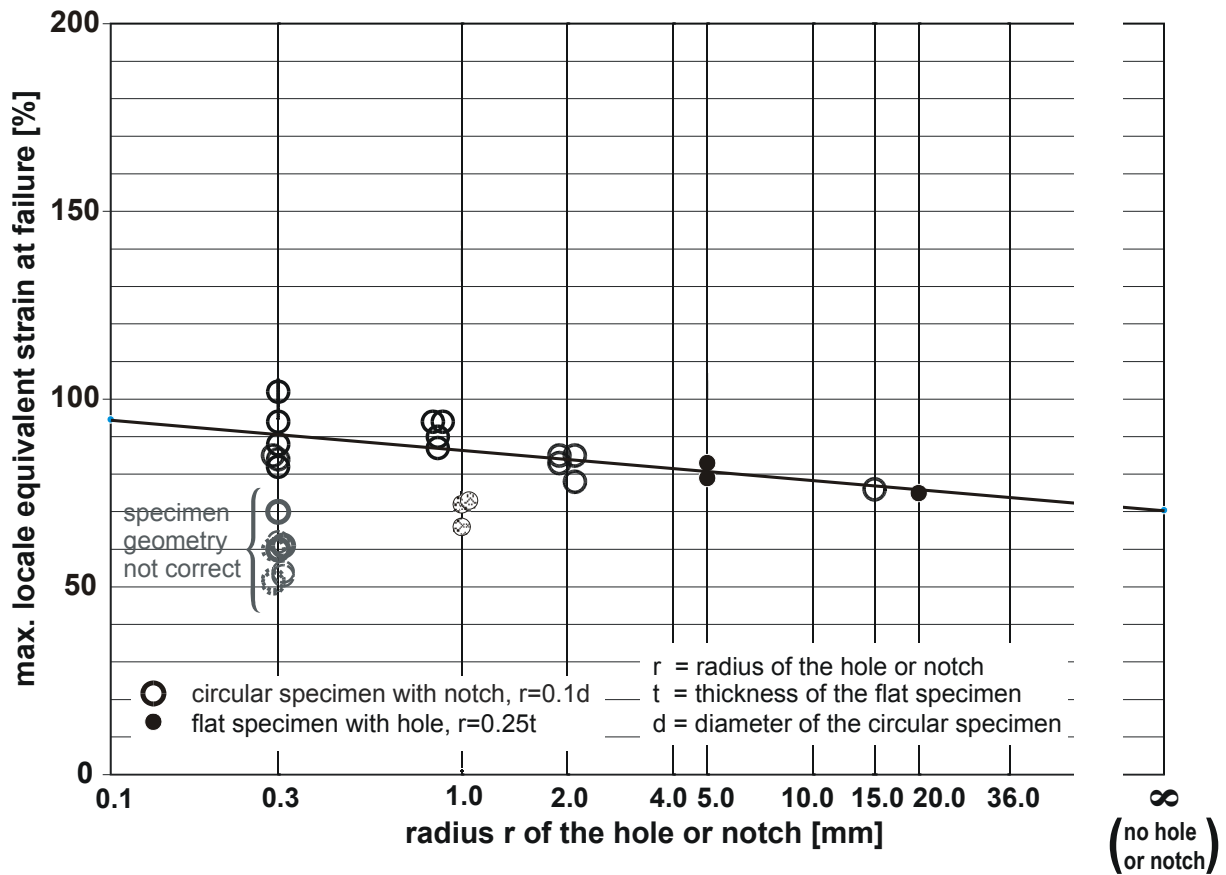


Fig. 19: Main results of LISSAC for RPV material at 850 °C, static tests

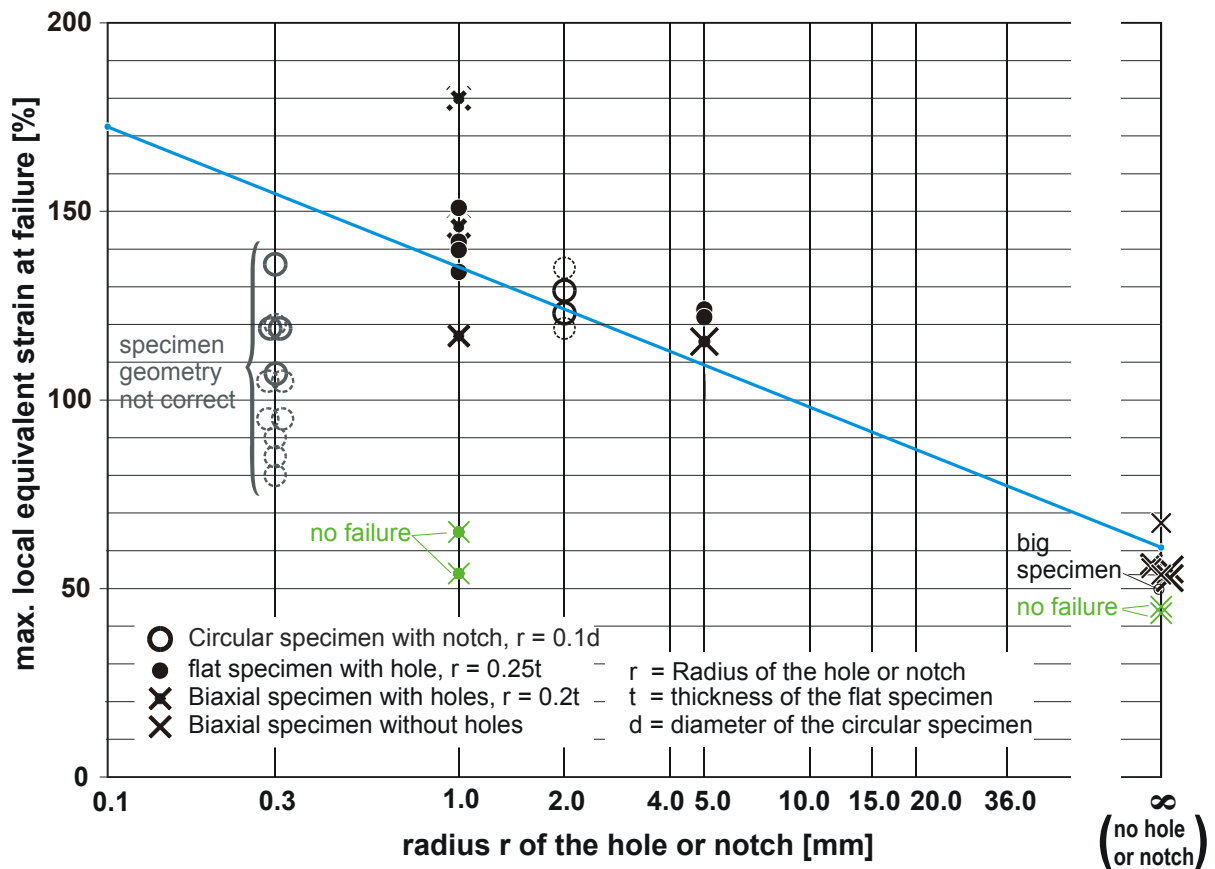


Fig. 20: Main results of LISSAC for RPV material at room temperature, dynamic tests

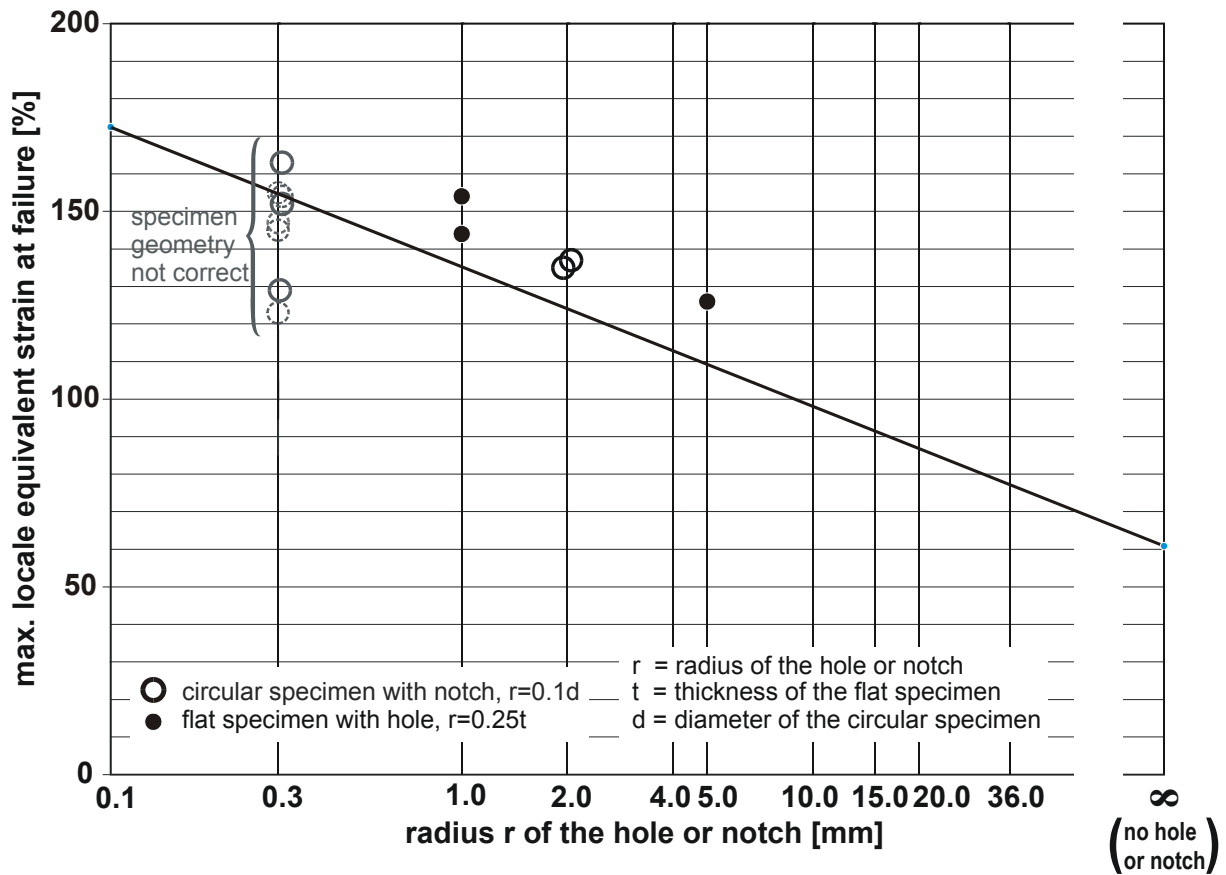


Fig. 21: Main results of LISSAC for RPV material at 400 °C, dynamic tests

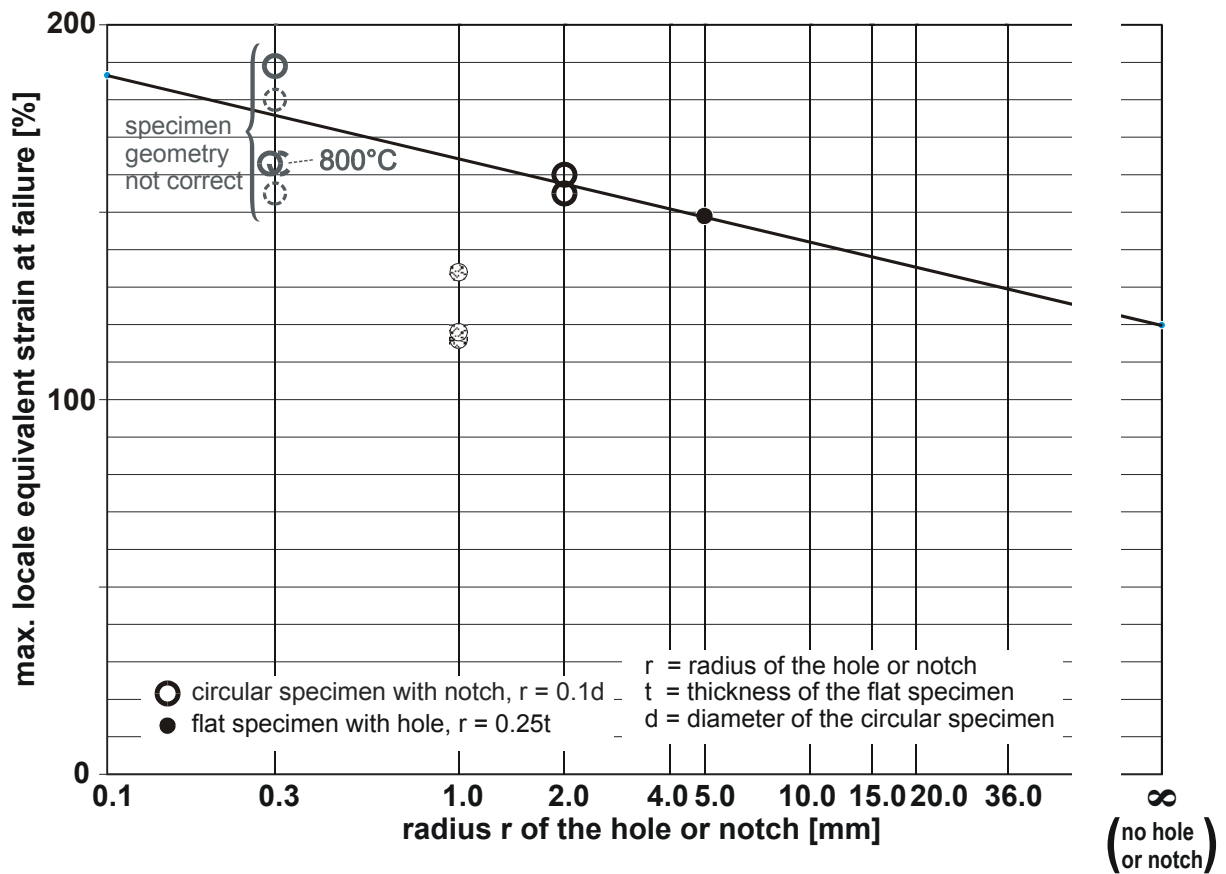


Fig. 22: Main results of LISSAC for RPV material at 850 °C, dynamic tests

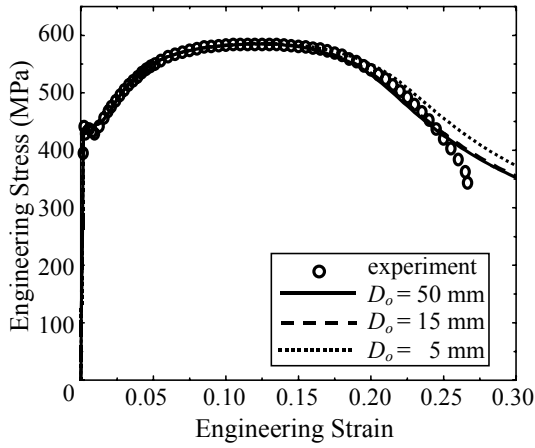


Fig. 23: Size effect on the engineering stress vs. engineering strain graph at the symmetry cross section, for geometrically similar tensile specimens without damage.

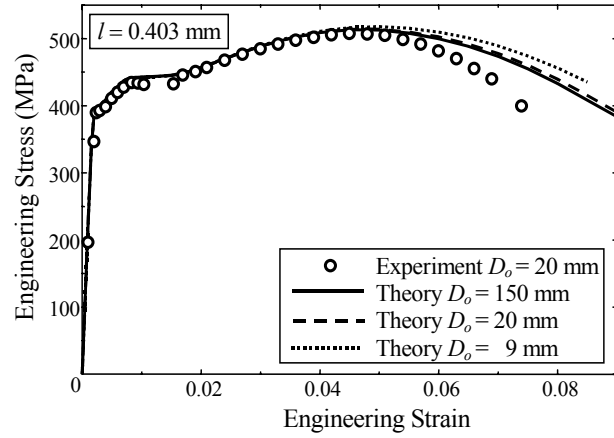


Fig. 24: Size effect on the engineering stress vs. engineering strain graph at the symmetry cross section, for geometrically similar notched tensile specimens without damage.

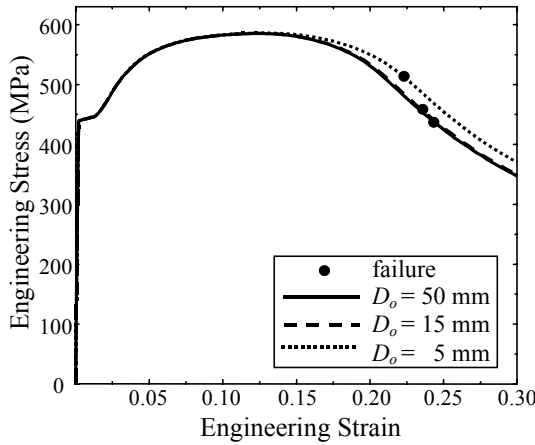


Fig. 25: Size effect on the engineering stress vs. engineering strain graph at the symmetry cross section, for geometrically similar tensile specimens, damage failure criterion $D_c = 0.05$.

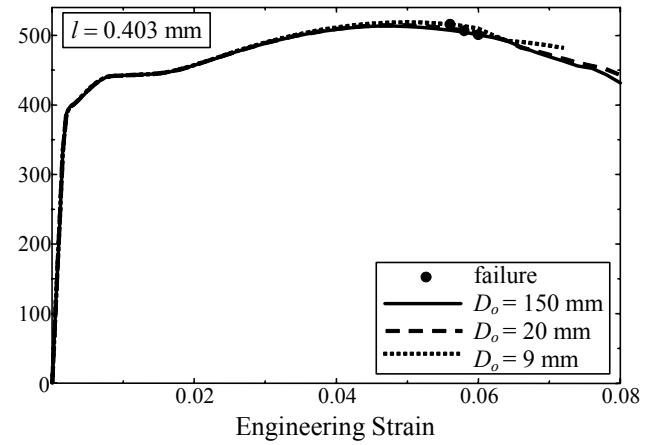


Fig. 26: Size effect on the engineering stress vs. engineering strain graph for geometrically similar notched specimens, damage failure criterion $D_c = 0.05$.

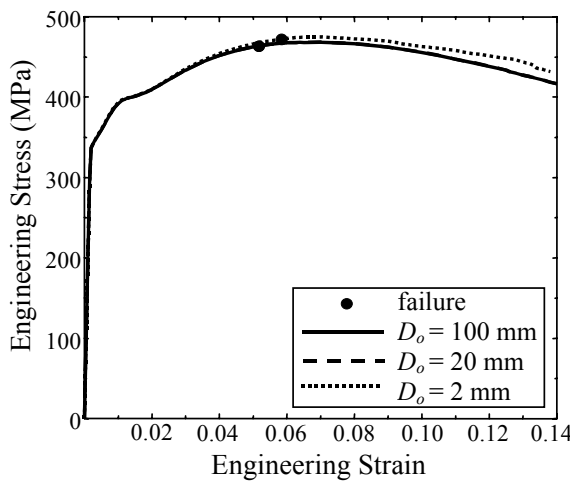


Fig. 27: Size effect (a) on the engineering stress vs. engineering strain relation for geometrically similar flat specimens with central hole damage failure criterion $D_c = 0.05$.

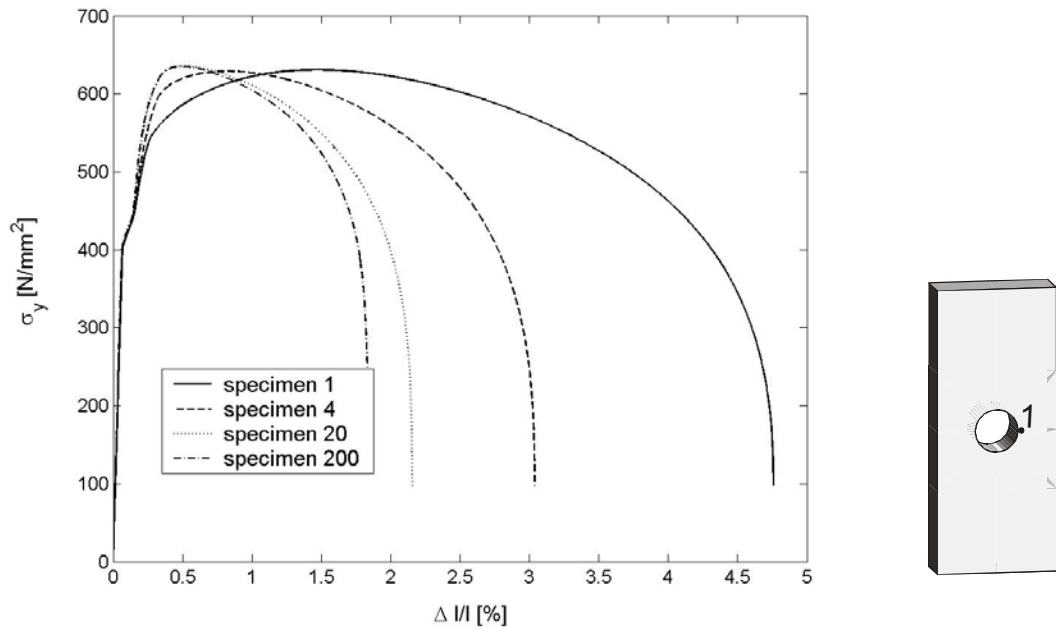


Fig. 28: σ_y at point (1) versus global strain - variation of the specimen's size (plasticity with scalar-valued damage)

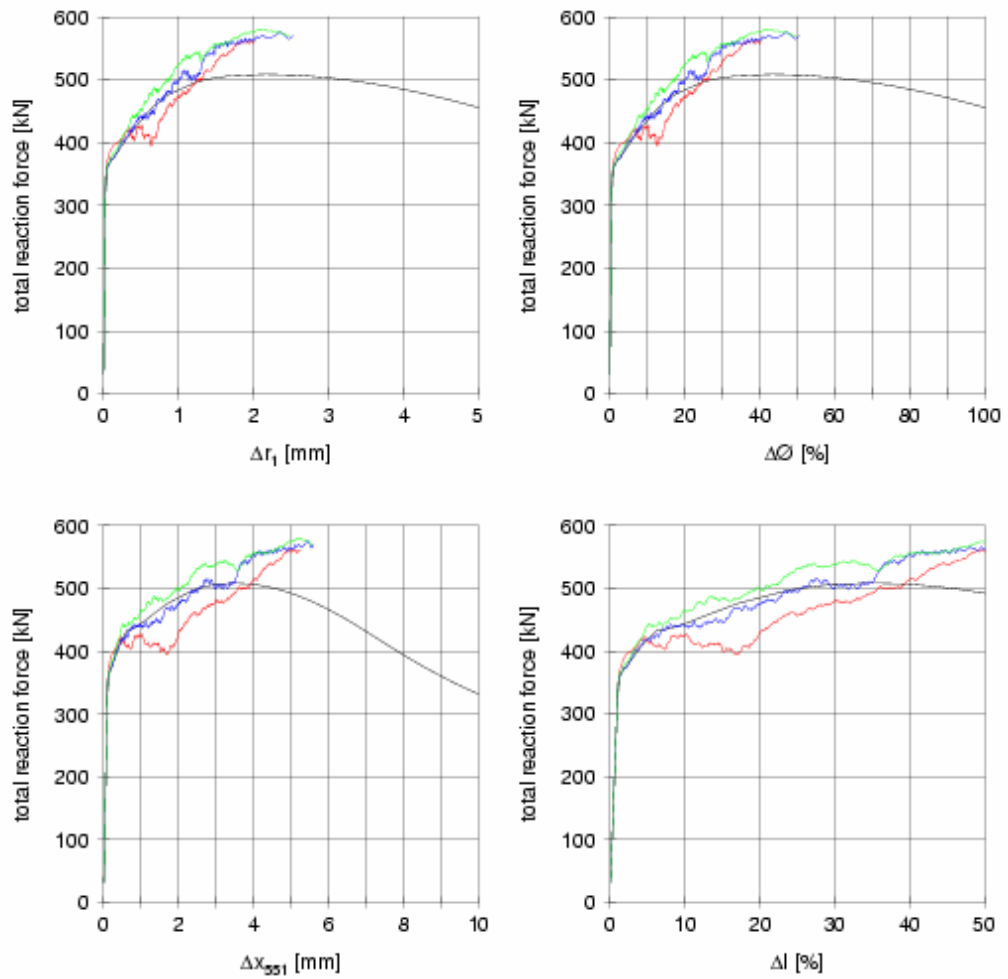


Fig. 29: Results for different sizes (0.2 mm, 20. mm and 200 mm thickness) of specimens

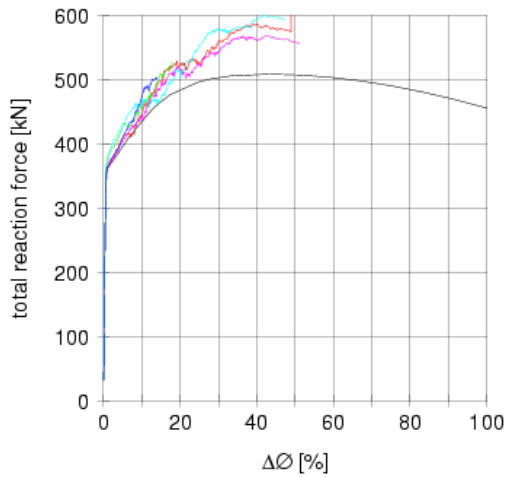


Fig. 30: Comparison of repeated calculations for 20 mm thick specimens

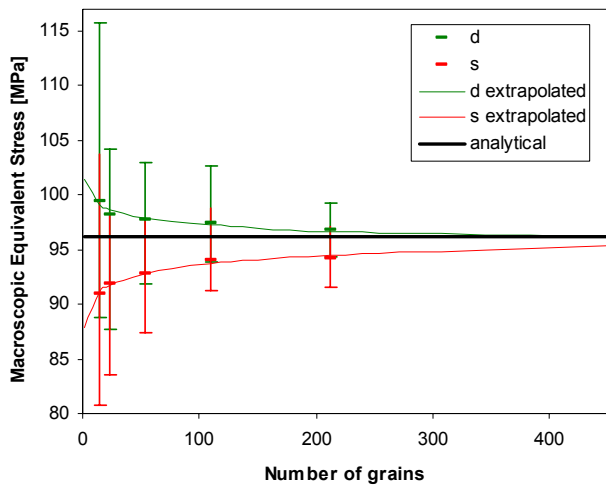


Fig. 31: Macroscopic equivalent stresses and scatter in **elasticity** depending on number of grains in polycrystalline aggregate for displacement (denoted as d) and stress (denoted as s) driven boundary conditions

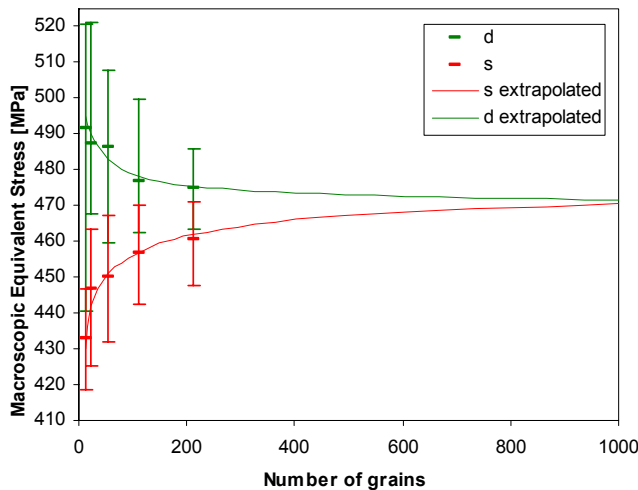


Fig. 32: Macroscopic equivalent stresses and scatter in **plasticity** depending on number of grains in polycrystalline aggregate for displacement (denoted as d) and stress (denoted as s) driven boundary conditions

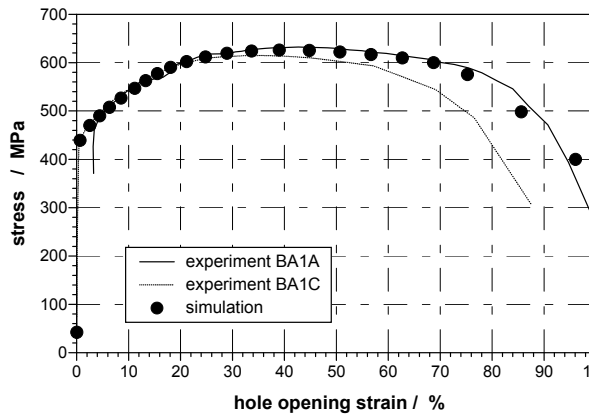


Fig. 33: Experimental and simulated stress of the flat specimens, hole diameter 2 mm

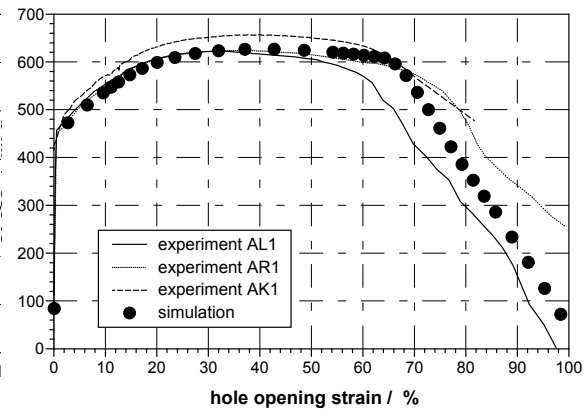


Fig. 34: Experimental and simulated stress of the flat specimens, hole diameter 10 mm

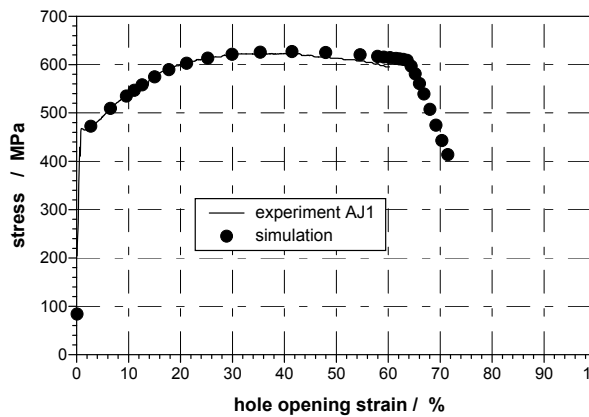


Fig. 35: Experimental and simulated stress of the flat specimens, hole diameter 20 mm

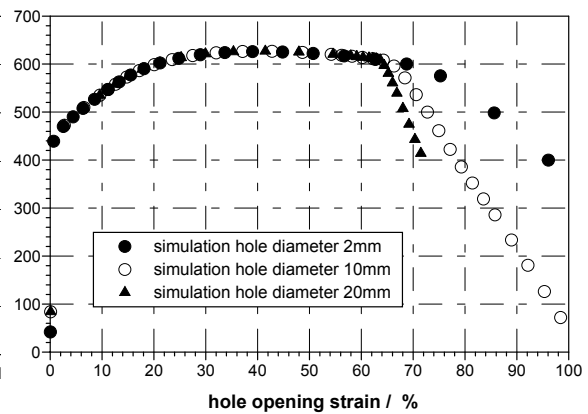


Fig. 36: Simulated stress of the flat specimens, with different sizes

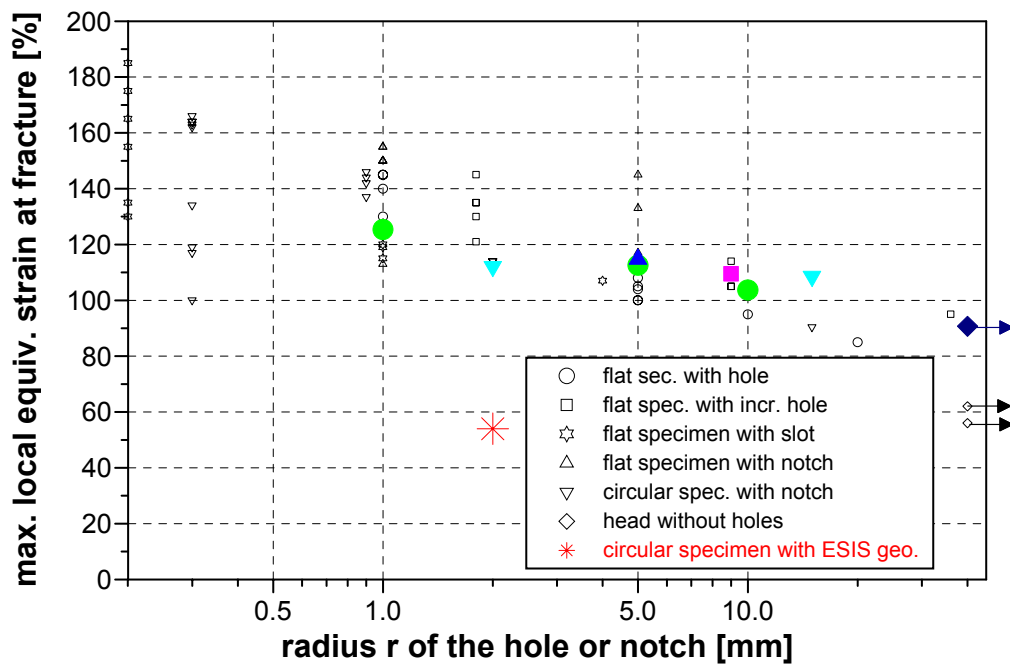


Fig. 37: Numerical (large symbols) and experimental (small symbols) max. local equivalent plastic strain at fracture initiation in dependence of the hole or notch radius

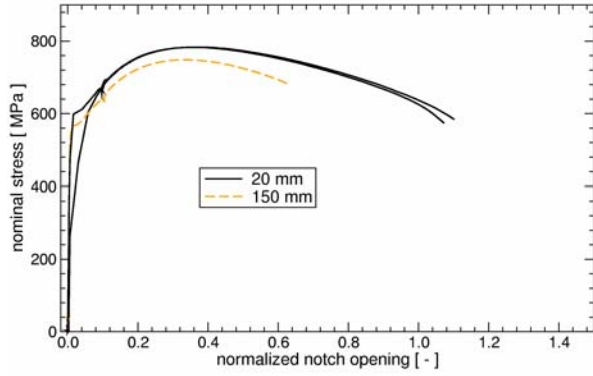


Fig. 38: Measured normalized notch opening of the round specimens with a notch

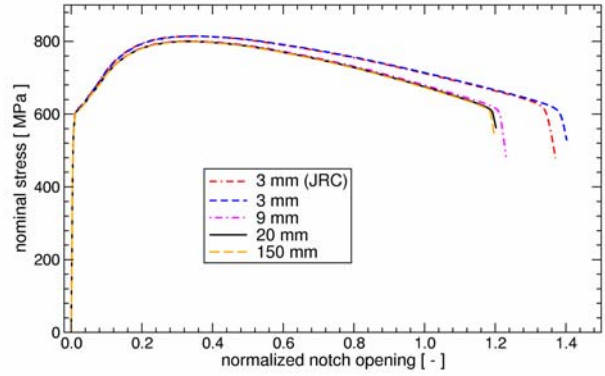


Fig. 39: Calculated normalized notch opening of the round specimens with a notch

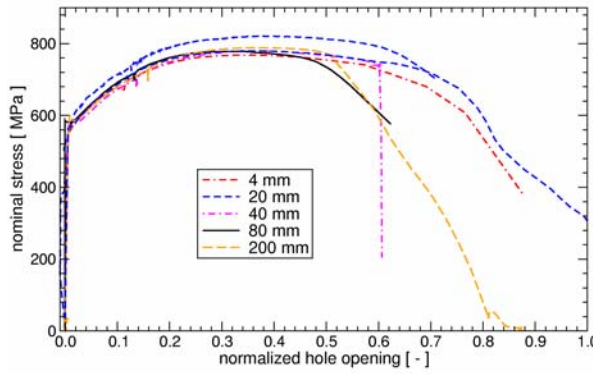


Fig. 40: Measured normalized hole opening of the flat specimens with central hole

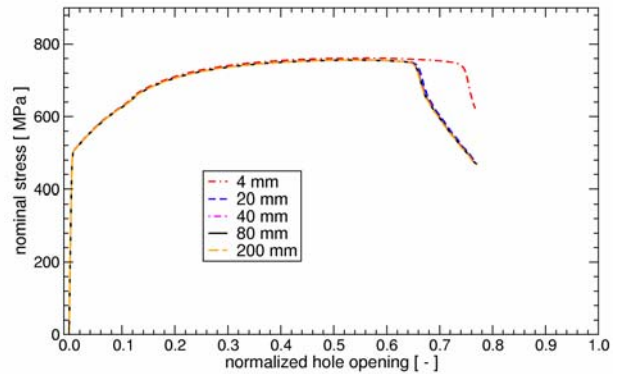


Fig. 41: Calculated normalized hole opening of the flat specimens with central hole

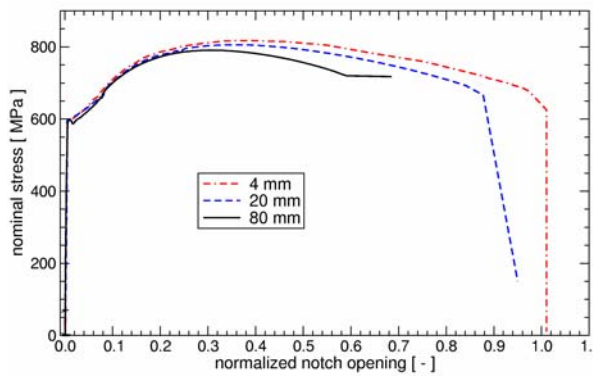


Fig. 42: Measured normalized notch opening of the flat specimens with a double edge notch

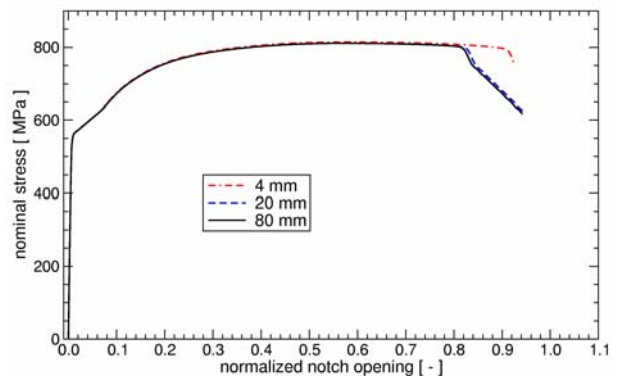


Fig. 43: Calculated normalized notch opening of the flat specimens with a double edge notch

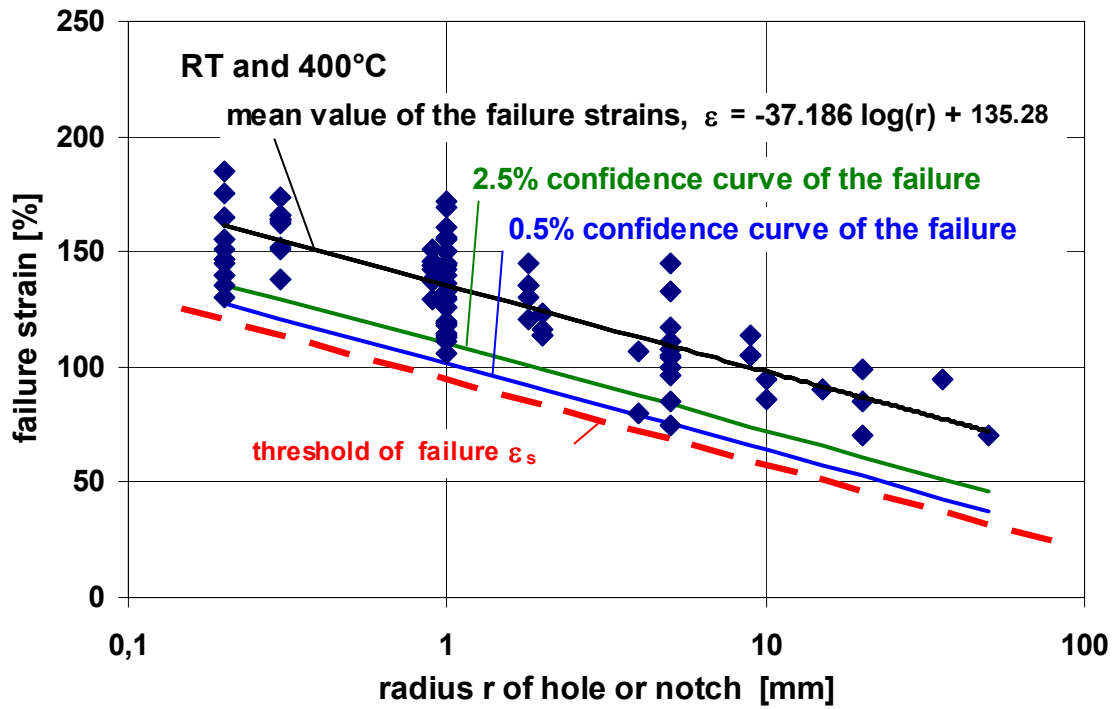


Fig. 44: Prediction confidence curves for the obtained failure strains

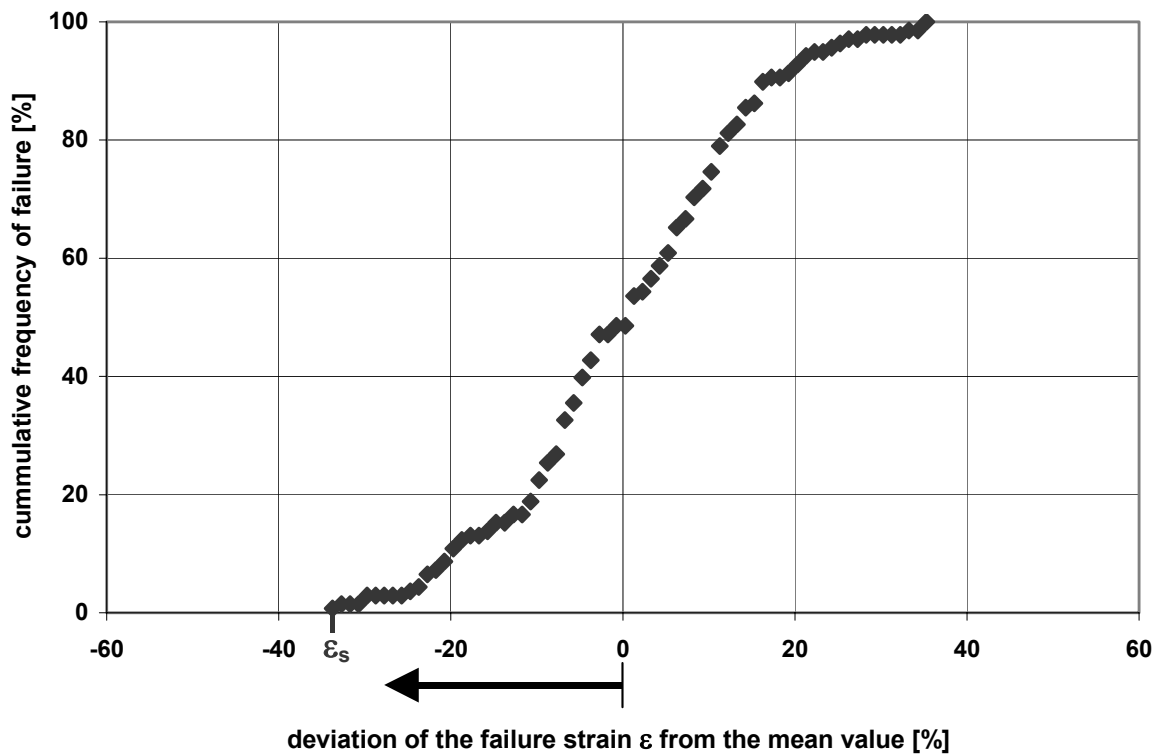


Fig. 45: Distribution of the probability of failure

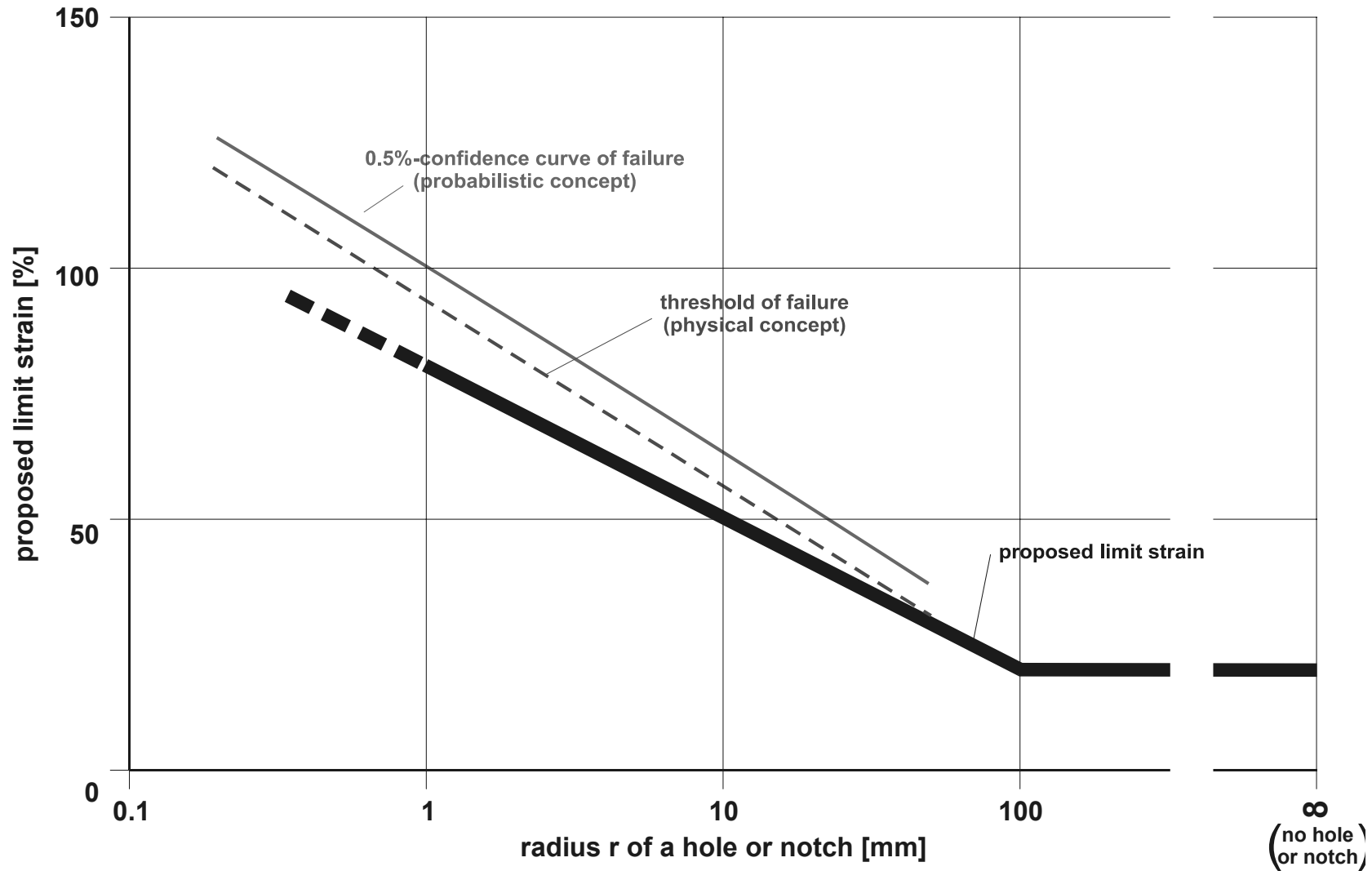


Fig. 46: Proposed limit strains for static and dynamic loading at room temperature and 400 °C

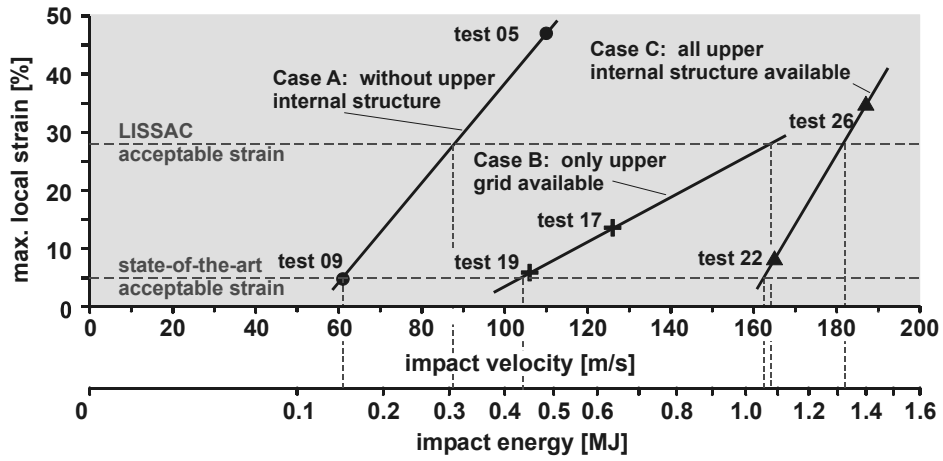


Fig. 47: Maximum local strain versus impact velocity or impact energy, respectively. For different acceptable strains (state-of-the-art: 5 %; LISSAC: 28 %), different admissible energies are obtained.

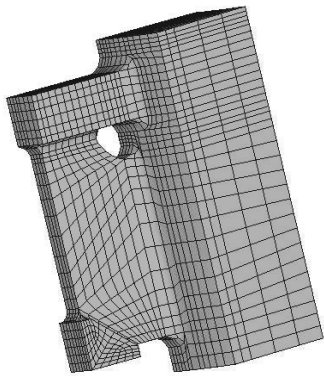


Fig. 48: Finite element model of the support pad with an adjacent section of the pressure vessel

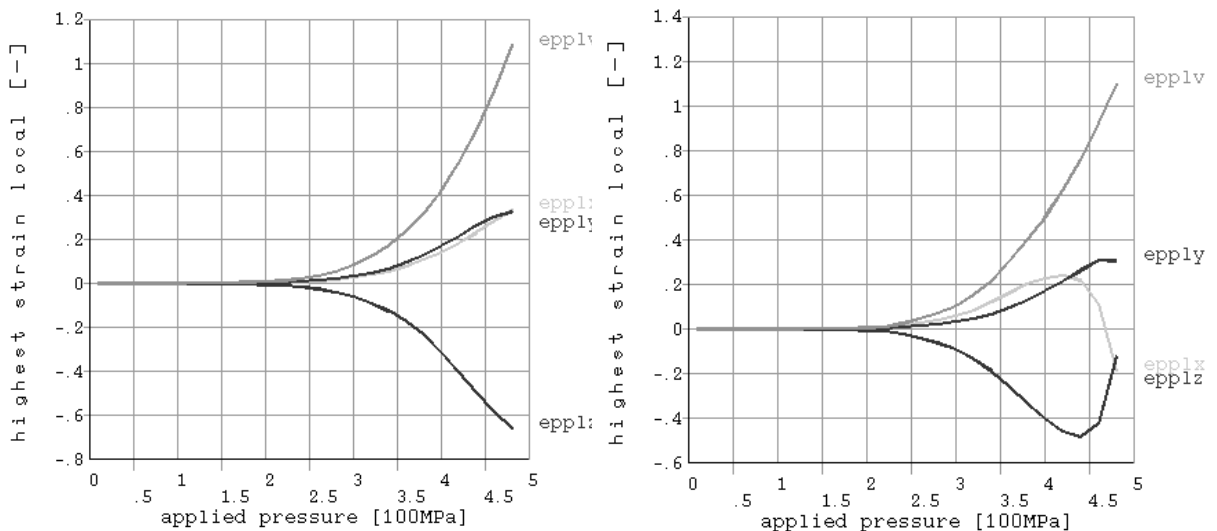


Fig. 49: Maximum local equivalent strain versus applied pressure elastic-plastic analysis
 Left: Pressure load at the top; Right: Pressure load at the bottom
 (epp1v: equivalent strain; epp1x, epp1y, epp1z: strain components)